# Modulation of large-scale structures by neutrally buoyant and inertial finite-size particles in turbulent Couette flow

Guiquan Wang,[1,2,3,*] Micheline Abbas,[2,3,†] and Eric Climent[1,3,‡]
[1]*Institut de Mécanique des Fluides de Toulouse (IMFT), Université de Toulouse, CNRS-INPT-UPS, Toulouse, France*
[2]*Laboratoire de Génie Chimique, Université de Toulouse, CNRS-INPT-UPS, Toulouse, France*
[3]*FERMaT, Université de Toulouse, CNRS, INPT, INSA, UPS, Toulouse, France*
(Received 13 December 2016; published 11 August 2017)

Particle-resolved numerical simulations based on the Force Coupling Method are carried out to study the effect of finite-size particles on turbulent plane Couette flow. The Reynolds number is close to the laminar-turbulent transition, such that large-scale rotational structures are well developed and self-sustained. The study particularly considers the effect of concentration, particle size, and particle-to-fluid density ratio on the mixture flow features. Time-averaged profiles, in the wall-normal direction, of the mean flow and Reynolds stress components reveal that there is no significant difference between single-phase and two-phase flows at equivalent effective Reynolds number, except that the wall shear stress is higher for the two-phase flow. However, temporal and modal analysis of flow fluctuations suggest that besides injecting small-scale perturbation due to their rigidity, particles have an effect on the regeneration cycle of turbulence. Indeed, the shape of the streaks and the intermittent character of the flow (amplitude and period of oscillation of the modal fluctuation energy) are all altered by the particle presence, and especially by the inertial ones.

DOI: 10.1103/PhysRevFluids.2.084302

## I. INTRODUCTION

Particulate flows are ubiquitous in industrial applications (mixing, transport, fluidization), in engineering like petroleum or chemical processes, food or solid processing, and water treatment. The transport of mixtures is often realized under a turbulent regime, especially at large scales. Under a turbulent regime, it is known that the dispersed phase (particles, bubbles, droplets) modulate transport properties of dispersed flows (see the review by Balachandar and Eaton [3] for turbulent flows laden with solid particles). The mechanisms of turbulence modulation by particles depend on many parameters (flow geometry, particle size, concentration, flow, and particle inertia), and they are still not completely elucidated over the entire parameter space.

Turbulence modulation by inertial particles (typically in gas-solid flows) results from a competition between drag-induced local dissipation and enhanced velocity fluctuations due to wake dynamics and self-induced vortex shedding. In summary, these phenomena depend predominantly on the size ratio between the particle diameter $d$ and characteristic flow length scales, the macro- and microscales being set respectively by the flow geometry and bulk Reynolds number. In a review of works carried out between 1971 and 1988, Gore and Crowe [20] established a qualitative relationship between the flow turbulent intensity and the ratio $d/l_e$ ($l_e$ being the flow integral length scale). A critical ratio $d/l_e \approx 0.1$ was found above (resp. below) which turbulence enhancement (resp. reduction) occurs. Flow modulation depends on $d/\eta$ ($\eta$ being the flow microscale) in a less obvious way. Pan and Banerjee [48] have shown through numerical simulations based on two-way

*gwang4academy@gmail.com
†Micheline.Abbas@ensiacet.fr
‡ecliment@imft.fr

 

coupling that, at small particle Reynolds numbers, the increase (resp. decrease) of turbulence intensity occurs for $d/\eta > 1$ (resp. $d/\eta < 1$). However, Burton and Eaton [7] who performed fully resolved simulation of homogeneous isotropic turbulence around a fixed particle with $d/\eta = 2$ showed reduction of the turbulence kinetic energy (TKE) within $1.5d$ of the particle surface but negligible turbulence modification outside a layer of $5d$ from the particle surface. A large number of works on this subject can be found in the literature, showing that modification of flow fluctuating energy varies with the wavelength compared to the particle size, and can depend on the direction and on the eventual location of the vortical structures with respect to a wall. It is out of the scope of the paper to make an exhaustive review of that, so we reference only few contributions: see Refs. [18,32,57,63,73].

The effect of neutrally buoyant particles on turbulent flow is different because there is no mean slip between phases. Dissipation and velocity fluctuations are both increased due to the perturbation of locally strained flow by particle rigidity. Among the few studies realized with neutrally buoyant particles Rashidi *et al.* [51] made measurements in turbulent channel flow at low concentration, with different particle sizes. They found that large particles increase the number of wall ejections, leading to higher turbulent intensities and Reynolds stress, while the opposite was observed for smaller particles. Recently, with the fast development of computer power and resources, a few studies considered the simulation of turbulent suspension flow with finite-sized particles. In addition to the conclusion of Ref. [51], Shao *et al.* [61] found a reduction of the intensity of the large-scale streamwise vortices by particles carried inside these structures, whereas other particles not carried by these structures induce small-scale perturbation that hinder the development of the large-scale streamwise vortices. Meanwhile, an increasing number of smaller-scale structures are induced. Their conclusions are done for suspension flows with low concentration up to 7%. Recently, Picano *et al.* [49] performed particle-resolved numerical simulations of turbulent channel flow at higher concentration (up to 30%) and focused on the effect of particles on the overall drag. They showed that when the concentration increases, the friction on the walls is increased, mainly from the increase of particle stress, while turbulent activity is reduced.

Close to laminar-turbulent transition, the presence of particles can advance or delay the transition from one regime to another. The experiments of Matas *et al.* [40] revealed that the effect of neutrally buoyant particles on the onset of turbulence in a pipe flow is non monotonous when the particle size and/or concentration is increased. Recent numerical studies [34,37,70] have shown a significant impact of large particles on the unsteady nature of pressure-driven flows, enhancing transverse turbulent stress components and modifying the flow vortical structures.

While the lifetime and shape of large-scale vortices (LSVs) in pressure-driven flows are strongly unsteady, turbulent plane Couette flow (pCf), close to the transition threshold, offers steady pairs of counter-rotating LSVs, which size is comparable to the Couette gap width. Near the wall, the large vortices generate ejection and sweep flows in the wall-normal direction that constitute the large-scale streaks (LSSs). These two structures permanently exchange energy and play a key role in the self-sustained turbulence process, so-called regeneration cycle [67]. In a minimal pCf unit, one can isolate a pair of LSVs, without affecting the regeneration cycle [24]. This allows us to study the impact of particles-vortices interaction on the regeneration cycle and thereby the turbulent flow features. We are interested in the modulation of large-scale structures by finite-sized particles. We consider first neutrally buoyant particles. Studies dedicated to turbulent pCf laden with finite-sized particles are scarce. In addition to being transported by the local fluid flow, neutrally buoyant finite-sized particles are subject to inertial migration (across flow streamlines) at large Reynolds numbers. Therefore its wall-normal motion results from a competition between repulsive turbulent ejection and inertial migration away from the Couette walls, against attractive turbulent sweep towards the wall, and turbulent or shear-induced dispersion. All this leads to possible heterogeneity in the particle distribution. The effect of a particle-to-fluid density mismatch is also interesting from a fundamental point of view (with zero average slip between dispersed and fluid phases, no effect of gravity). It is known that particles denser than the fluid tend naturally to accumulate in low strain rate regions of a vortex, whereas lighter particles have an inward motion towards the vortex center. Klinkenberg *et al.* [30] observed that inertial point particles ($d/\eta < 1$) induce a significant time delay

on the streak breakdown which may cut off the regeneration cycle near the transition threshold. In highly turbulent flows, less inertial point particles collect into low-speed streaks, especially in the small-scale hairpin vortices corresponding to Q2 events [53–55]. This leads to an increase in the streamwise fluctuating velocity, while spanwise and wall-normal velocity fluctuations are damped. However, heavy particles are confined in the high-speed streak. They reduce near-wall swirling motion, which in turn results in a reduction of the turbulent Reynolds stress.

In this context, we aim at investigating numerically the properties of turbulent pCf laden with finite-size particles. Particles 10 to 20 times smaller than the LSVs are considered. The particle concentration investigated in this work is low to moderate ($\phi \leqslant 10\%$), and the Reynolds number of the Couette flow is relatively low $\mathrm{Re}_b = 500$ based on the fluid viscosity. The paper is organized as follows. In Sec. II particular features of the Force-Coupling Method used to simulate the suspension flow dynamics, and some validations are outlined. In Sec. III the effect of neutrally buoyant particles on statistical properties of the turbulent flow (velocity profile, concentration distribution, turbulence intensity, shear stress) are discussed. In Sec. IV we consider the effect of the particle-to-fluid density ratio (ranging from zero to five) on the flow properties. Finally, the effect of particles on the regeneration cycle is discussed, using modal and quadrant analysis and vorticity stretching. The paper ends with a conclusion on the main findings.

## II. SIMULATION METHOD AND VALIDATION

Direct numerical simulations of single-phase flows are performed by using the code JADIM for an incompressible Newtonian fluid [8]. The unsteady 3D Navier-Stokes equations discretized on a staggered grid are integrated in space using the finite volume method. All terms involved in the balance equations are written in a conservative form and are discretized using second-order centered schemes in space. The solution is advanced in time by a second-order semi-implicit Runge-Kutta combined to Cranck Nicholson time-stepping procedure, and incompressibility is achieved by correcting the pressure contribution, which is a solution of the Poisson equation.

Numerical simulations of particle trajectories and suspension flow dynamics are based on multipole expansion of momentum source terms added to the Navier-Stokes equations [namely, the Force-Coupling Method (FCM) as described in Refs. [12,39,43]], the comparison of FCM with other methods that belong to the class of Fictitious Domain methods can be found in a review by Maxey [42] on the simulation methods for particulate flows. Flow equations are dynamically coupled to Lagrangian tracking of particles. The fluid is assumed to fill the entire simulation domain, including the particle volume. The fluid velocity and pressure fields are a solution of continuity [Eq. (1)] and momentum balance [Eq. (2) and Eq. (3)]:

$$\nabla \cdot \boldsymbol{u} = 0, \tag{1}$$

$$\rho \frac{D\boldsymbol{u}}{Dt} = -\nabla p + \mu \nabla^2 \boldsymbol{u} + \boldsymbol{f}(\boldsymbol{x},t), \tag{2}$$

$$f_i(\boldsymbol{x},t) = \sum_{n=1}^{N_p} F_i^n \triangle[\boldsymbol{x} - \boldsymbol{Y}^n(t)] + G_{ij}^n \frac{\partial}{\partial x_j} \triangle'[\boldsymbol{x} - \boldsymbol{Y}^n(t)]. \tag{3}$$

The body force distribution $\boldsymbol{f}(\boldsymbol{x},t)$ in the momentum balance (3) accounts for the presence of particles in the flow. It is written as a multipole expansion truncated after the second term. The first term of the expansion called the monopole represents the force $\boldsymbol{F}^n$ that the particle exerts on the fluid, due to particle inertia, external forcing, or particle-to-particle contact forces [Eq. (4)]. The second term, called dipole, is based on a tensor $\boldsymbol{G}^n$ sum of two contributions: an antisymmetric part is related to external torques applied on the particle, and a symmetric part that accounts for the resistance of a rigid particle to deformation by ensuring zero average strain-rate inside the particle

volume [Eq. (5)]:

$$\boldsymbol{F}^n = (m_p - m_f)\left(\boldsymbol{g} - \frac{d\boldsymbol{V}^n}{dt}\right) + \boldsymbol{F}^n_{\text{ext}}, \tag{4}$$

$$S^n_{ij}(t) = \frac{1}{2}\int \left(\frac{\partial u_i}{\partial x_j} + \frac{\partial u_j}{\partial x_i}\right)\triangle'[\boldsymbol{x} - \boldsymbol{Y}^n(t)]\, d^3x = 0. \tag{5}$$

The particle finite size is accounted for by spreading the momentum source terms around the particle center $\boldsymbol{Y}^n$ using a Gaussian spherical envelope, one for the monopole $\triangle(\boldsymbol{x}) = (2\pi\sigma^2)^{-3/2}e^{(-|\boldsymbol{x}|/2\sigma^2)}$, and another one for the dipole $\triangle'(\boldsymbol{x}) = (2\pi\sigma'^2)^{-3/2}e^{(-|\boldsymbol{x}|/2\sigma'^2)}$. The widths of the Gaussian envelopes, $\sigma$ and $\sigma'$, are set with respect to the particle radius $a$ such that the settling velocity and the hydrodynamic perturbation generated by a particle in a shear flow are both exactly matched to Stokes solutions [$\sigma = a/\sqrt{\pi}$ and $\sigma' = a/(6\sqrt{\pi})^{1/3}$] for a single particle.

The particle translation and rotation velocities are obtained from a local weighted average of the volumetric fluid velocity (resp. rotational velocity) field over the region occupied by the particle:

$$\boldsymbol{V}^n(t) = \int \boldsymbol{u}(\boldsymbol{x},t)\triangle[\boldsymbol{x} - \boldsymbol{Y}^n(t)]\, d^3x = 0, \tag{6}$$

$$\Omega^n(t) = \frac{1}{2}\int [\nabla \times \boldsymbol{u}(\boldsymbol{x},t)]\triangle'[\boldsymbol{x} - \boldsymbol{Y}^n(t)]\, d^3x = 0. \tag{7}$$

Particle trajectories are then obtained from numerical integration of the equation of motion:

$$\frac{d\boldsymbol{Y}^n}{dt} = \boldsymbol{V}^n. \tag{8}$$

This modeling approach allows calculating the hydrodynamic interactions with a moderate computational cost. In order to capture correctly the dynamics of dilute suspension flows, four grid points per particle radius are usually required when the monopole force is not zero, and in the case where only dipole forcing is relevant, three grid points per particle radius are sufficient.

For neutrally buoyant particles, the only contribution to the monopole is $\boldsymbol{F}^n_{\text{ext}}$ due to rigid body contact forces. For a pair of particles $\alpha$ and $\beta$, a force derived from a repulsive potential is added to the monopole term of both particles [such as Eq. (4) for particle $\alpha$] when the distance between particles is smaller than $R_{\text{ref}} - 2a$ and zero otherwise. Following Abbas *et al.* [1], this force is written as

$$\boldsymbol{F}^{\alpha,\beta}_{\text{ext}} = F_{\text{ref}}\left[\frac{R^2_{\text{ref}} - (r^{\alpha,\beta})^2}{R^2_{\text{ref}} - (2a)^2}\right]\frac{\boldsymbol{x}^{\alpha,\beta}}{2a}. \tag{9}$$

$F_{\text{ref}}$ is scaled with the Stokes drag force $F_d = 6\pi\mu\gamma a^2$ based on characteristic particle relative velocity in shear flow $\gamma a$ where $\gamma$ is the shear rate. The value of the force barrier during a collision is set in response to the proximity of the particles. The total force is obtained through a pairwise summation procedure.

The relative trajectories of two colliding particles in laminar Couette flow are shown in Fig. 1. The particles were placed initially in the flow velocity gradient plane. Their relative initial position was set outside the area where closed relative trajectories might be observed (see Refs. [21,33]). A condition for utilizing this simplified model is that there is no elastic or inelastic collisions when contacts between particles happen. As demonstrated in Ref. [15], a no-rebound situation exists during the collision under the condition of $\text{St} < 10$ where the particle impact Stokes number St compares particle inertial effect to viscous effect. All values $\text{St}_{(\text{max})}$ (shown in Table II for this work) are below this critical value. Figure 1 shows that particles do not overlap when the repulsive force is activated for either bubbles or neutrally buoyant or inertial particles.

At higher volume fractions it is necessary to provide a more detailed representation including viscous lubrication forces and solid-body contact forces. In principle, viscous lubrication forces

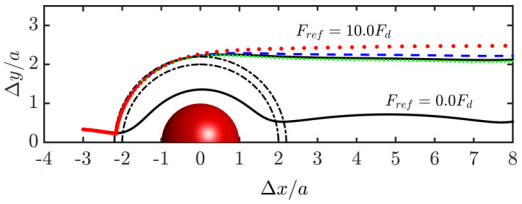


FIG. 1. Relative trajectory of a particle pair in laminar Couette flow, in the case of neutrally buoyant or inertial particles and bubbles. The red half sphere represents the reference particle. The semicircle of radius $2a$ is the limit of particle overlapping. The other semicircle indicates the barrier corresponding to $R_{\text{ref}} = 2.2a$ where the repulsion force is enabled. The particle $\text{Re}_p \equiv \gamma a^2/\nu = 1.0$ and $\text{St} \equiv (2\text{Re}_p\rho_p)/(9\nu\rho_f)$ varies between 0.2 and 2. —— neutrally buoyant particle; - - - $\rho_p/\rho_f = 5$; • $\rho_p/\rho_f = 10$; ..... bubble.

will prevent contact of perfectly smooth particles, but contact occurs in practice through surface roughness. Tests were made, varying the magnitude of the force $F_{\text{ref}}$ and the cutoff distance $R_{\text{ref}}$. In turbulent flow simulations, $F_{\text{ref}}$ was chosen such that the number of overlapping particles was found to be less than 1% of the total particle number ($F_{\text{ref}}/F_d = 10$) at the largest concentration ($\Phi = 10\%$).

### A. Validation of FCM

In the absence of external forces (no gravity effect for neutrally buoyant particles), the coupling between the particles and the carrier flow occurs exclusively from the force dipole term, which is mainly related to the local flow strain rate. Accordingly, the method has been validated under finite Reynolds number flow configurations. The dipole tensor computed for a particle in pure shear flow (negligible wall effect in wide-gap pCf) was validated (in Refs. [37,38]) against direct numerical simulation results reported in Ref. [46]. The comparison revealed that our method captures accurately the hydrodynamic perturbation when the particle Reynolds number is below 10. Also the equilibrium position of a particle in laminar pressure-driven flow due to cross-streamline inertial migration (Segré-Silberberg effect) agrees well with theoretical predictions in the same range of particle Reynolds numbers. In this paper, we show additional validation tests relevant to particles in Couette flow. First, the effect of increasing the particle-to-Couette gap size ratio, i.e., a particle confined between walls, is studied in the limit of low $\text{Re}_p$, where theoretical predictions exist. Second, particle wall-normal velocity is calculated, in a Couette flow, at low but finite flow inertia. Last, the effect of particle inertia is considered to test the unsteady response of a particle in a quiescent fluid experiencing an oscillatory force. In this latter configuration, FCM results are accurate as long as the Stokes layer of the velocity perturbation near the particle surface is not too thin. An additional configuration is reported in Appendix A where the Taylor-Green vortex array mimics to a certain extent the large-scale vortices in turbulent pCf.

#### *1. Effect of confinement on particle stresslet and rotation in laminar pCf*

The first configuration consists in a single neutrally buoyant particle, located at the center of a laminar pCf for low Reynolds number. The particle does not have any initial translation or rotational velocity, and its translational velocity remains zero because the flow velocity cancels at the gap center. However, particle rotation due to the shear flow vorticity converges in time to a steady value that depends on the Couette gap width. In the limit of wide gap, where the wall contribution to hydrodynamic perturbation is negligible, our previous tests have shown that the FCM response is accurate especially when the particle Reynolds number is lower than 10 ([37,38]). In the case of thin gap, short-range particle-wall interaction becomes important. Particle stresslet and rotational velocity are calculated numerically and compared to the theoretical predictions of Sangani *et al.* [59] based on Lamb multipoles (following the work of Ozarkar and Sangani [47]). In their work,

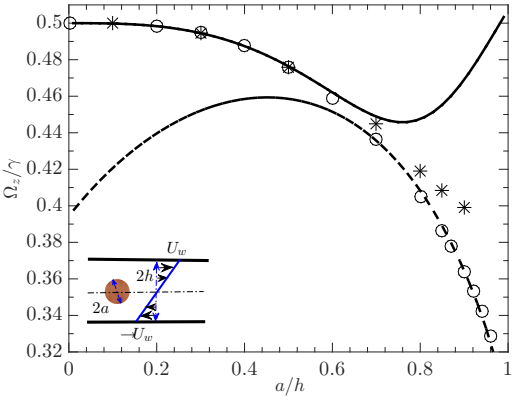


(a)

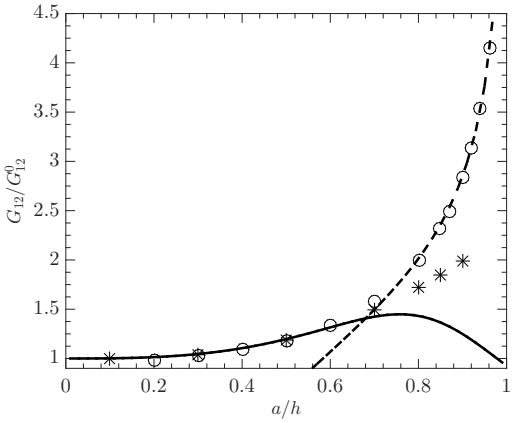


(a)

FIG. 2. (a) Rotational velocity and (b) stresslet of a neutrally buoyant sphere at the center of laminar pCf as a function of the ratio between the particle radius and half of the gap width $a/h$. The rotational velocity is scaled by the flow shear rate $\gamma$, and the stresslet is scaled by its value in unbounded shear flow $G_{12}^0 = \frac{10}{3}\pi\mu a^3\gamma$. The stars $*$ are obtained using FCM simulations at $\mathrm{Re}_p = 0.01$, and circles $\circ$ are from simulations of Sangani *et al.* [59] in Stokes flow. The lines are from asymptotic limits written in Ref. [59]: —— $a/h \ll 1$; – – – $0 \ll a/h < 1$.

the rotational velocity and stresslet are predicted for both asymptotic limits: $0 < a/h \ll 1$ and large $0 \ll a/h < 1$ particle-to-gap size ratio (where $h$ is half the Couette gap width).

As shown in Figs. 2(a) and 2(b), the confinement reduces the rotational velocity of the sphere and increases its shear stresslet when compared to its value for unbounded shear flow. The FCM response is accurate up to $a/h = 0.8$. The deviation observed for stronger confinement would need to be supplemented by adding higher order multipoles or lubrication correction. The largest discrepancy of FCM results compared to theoretical predictions is $\approx$4% and 10% for rotational velocity and stresslet, respectively, when the particle size is $a/h = 0.8$.

### *2. Wall-normal particle migration*

When a neutrally buoyant particle is not set in the midplane of the Couette gap, the asymmetry of velocity perturbation leads to a wall-normal force oriented towards the center of the gap, as long as the particle Reynolds number is not negligibly small (which breaks the flow reversibility argument). This was observed in the experiments of Ref. [22] in cylindrical Couette flow and later in the

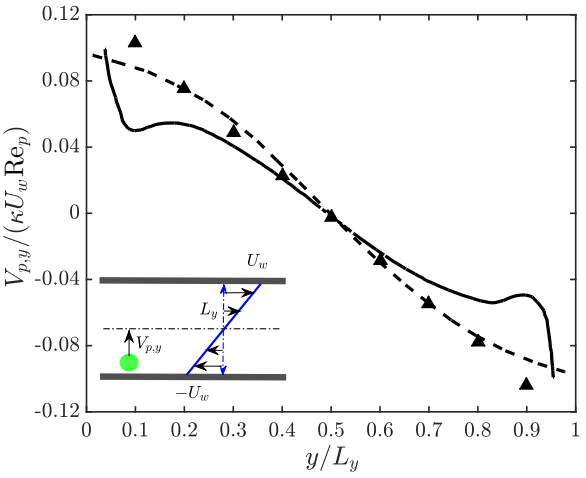


FIG. 3. Quasisteady wall-normal velocity of a single particle as a function of the particle distance to the wall in laminar pCf. The lines are theoretical predictions from Ref. [66] (dashed line) and Ref. [25] (solid line); ▲ present simulation with $\kappa = d/L_y = 1/32$, $\mathrm{Re}_p = 2.4 \times 10^{-4}$.

2D direct numerical simulation by Ref. [19]. Theoretical predictions were derived by Refs. [25,66], under quasisteady state, in the limit of finite particle size and low but finite particle Reynolds number (the wall falls inside the region perturbed by the particle). We tested the accuracy of the FCM under such conditions, using a Couette gap-to-particle diameter size ratio $L_y/d = 32$ and particle Reynolds number $\mathrm{Re}_p \equiv \frac{\gamma d^2}{4\nu} = 2.4 \times 10^{-4}$, where $\gamma$ is the shear rate and $\nu$ is the kinematic viscosity. Figure 3 shows the quasisteady dimensionless wall-normal migration velocity $\frac{V_{p,y}}{\kappa U_w \mathrm{Re}_p}$ where $\kappa = d/L_y$ is the ratio between particle diameter with Couette gap width. The numerical results are obtained after 100 iterations corresponding to $t\nu/a^2 = 1.5$, which are required for the convergence of the velocity while the wall-normal migration distance is still insignificant. The simulation results are in very good agreement with the theoretical predictions proposed by Ref. [66]. Near the wall, the method is less accurate. Higher orders are required in the multipole expansion to capture the lubrication effect. At higher particle Reynolds number, the wall-normal velocity is larger leading to effective particle migration towards the Couette center [the migration velocity scales as $O(\mathrm{Re}_p)$].

### 3. *Periodic oscillation of a single particle*

Turbulence has a wide range of length or time scales which exert forcing on particles. Large-scale vortices have strong forcing amplitudes but longer time scales, whereas small-scale vortices may generate higher frequency forcing on particles. As described by Climent and Maxey [11], FCM framework embeds drag, added-mass, lift, and history forces experienced by the particle in $\mathbf{F}^n$ [Eq. (4)]. In this section, we focus on the ability of FCM to model the unsteady response of a particle experiencing an oscillatory external force without considering gravity. Following Ref. [41], we consider the motion of a rigid (neutrally buoyant or dense) particle moving in a fluid that is otherwise quiescent. The solution of this problem is equivalent to that of an oscillating fluid obtained in a frame attached to the particle which generates the development of Stokes layer at the particle surface. Particle oscillation is imposed via temporal evolution of the monopole term $\mathbf{F}_{\mathrm{ext}}(t) = 6\pi\mu a\mathbf{u}_0 \sin(\omega t)$, where $\mathbf{u}_0$ is a constant vector. The velocity field induced by the particle is obtained by solving Eqs. (1)–(3), and the particle velocity $\mathbf{u}_p$ is obtained by integration of the local fluid velocity using Eq. (6). Snapshots of the velocity field are displayed in Fig. 4, for two values of $\delta^2 \equiv \omega a^2/\nu$, which is the ratio of the particle radius to the Stokes layer thickness. This figure shows that the flow velocity perturbation representing the Stokes layer thickness shrinks when the

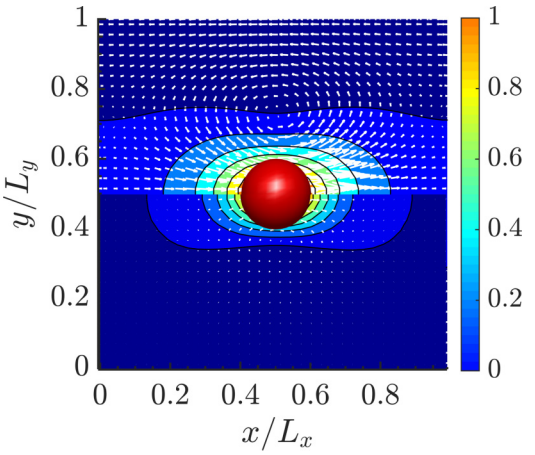


FIG. 4. Velocity field and contours of $u/u_p$ when $t = 0 + 2k\pi/\omega$ (top half: $\delta^2 = 0.25$, and bottom half: $\delta^2 = 4.0$ where $\delta$ stands for dimensionless Stokes layer) around an oscillatory particle.

oscillation frequency increases. Note that $\delta^2$ (as defined here) is equivalent to the ratio of particle relaxation to fluid characteristic oscillation time scale, and by consequence to a Stokes number.

The motion of the oscillating particle is written as

$$\mathbf{u_p}(t) = \alpha \mathbf{u_0} \sin(\omega t + \varphi), \tag{10}$$

where the velocity is proportional to the force amplitude and $\varphi$ is the phase shift.

FCM results are compared to that of Maxey-Riley equation [Eq. (A1)] following Ref. [44] which is valid in the limit of low particle Reynolds number. For quiescent fluid far from the particle, the analytical relationship between the amplitude of external oscillatory forcing [written as $F(t) = \widehat{F} e^{i\omega t}$] and particle velocity is

$$\widehat{F} = \widehat{u}_p \left[ \left( m_p + \tfrac{1}{2} m_f \right) i\omega + 6\pi\mu a (1 + \delta e^{i\pi/4}) \right] e^{i\varphi}. \tag{11}$$

The terms on the right-hand side of Eq. (11) correspond to particle inertia, added mass, and steady and unsteady drag forces. The Basset history force is important when the particle-to-fluid density ratio is low to moderate. The theoretical prediction of $\alpha$ and $\varphi$ as well as the FCM results [Eq. (11)] are displayed in Figs. 5(a) and 5(b) as a function of $\delta^2$. This figure shows that the modulus is calculated accurately up to $\delta^2 = 2.5$. The under-estimation of the phase lag increases when particle inertia decreases, and the maximum discrepancy with respect to Maxey-Riley's prediction is around 13% for the bubble case when $\delta^2 = 2.5$. The numerical simulations corresponding to turbulent plane Couette flow with the largest particles ($L_y/d = 10$) are carried out only with neutrally buoyant particles, in which case $\delta^2$ is less than 1.25 (7% discrepancy in the test case). As for the error corresponding to the small particle case ($L_y/d = 20$), its maximum value is around 5%, according to the oscillation test for the case of bubbles. At higher values of $\delta^2$, the Stokes layer is too thin to be accurately resolved by FCM. The purely viscous contribution of the hydrodynamic force (in the absence of added mass term) is also plotted in Figs. 5(a) and 5(b) for comparison. Furthermore, the effect of density ratio up to five is also investigated. It is clear that FCM predictions become gradually closer to the theoretical prediction while particle density is increased because the relative contribution of unsteady Basset drag reduces.

## III. SIMULATION OF SINGLE-PHASE TURBULENT PLANE COUETTE FLOW

The flow is driven by two infinite parallel plates moving in opposite directions. Periodic boundary conditions are set in streamwise and spanwise directions, and no slip condition is imposed at the

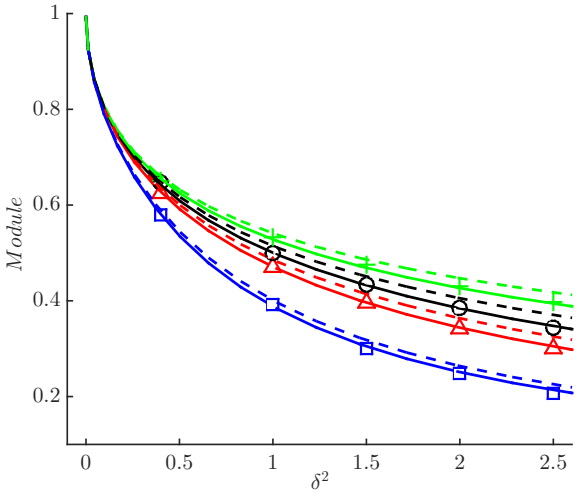


(a)

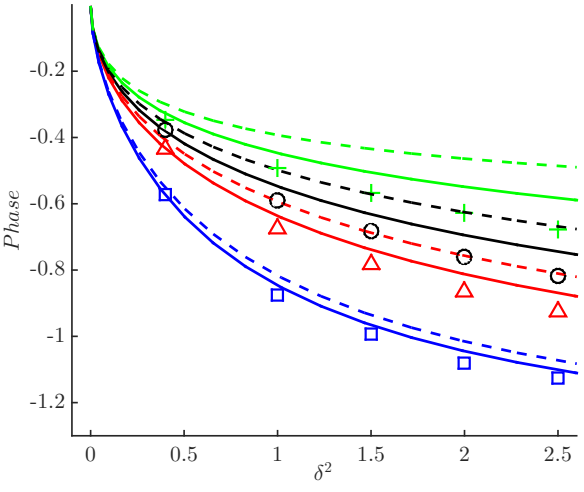


(b)

FIG. 5. (a) Amplitude and (b) phase shift of $6\pi a\mu\hat{u}_p/\hat{F}$ as a function of the dimensionless frequency ($\delta^2$). The lines are obtained from solving the Maxey-Riley equation (A1), with and without the added mass contribution (solid and dashed lines, respectively). The symbols are from present simulation of + bubbles; $\circ$ $\rho_p/\rho_f = 1$; $\triangle$ $\rho_p/\rho_f = 2$; $\square$ $\rho_p/\rho_f = 5$.

two walls. The domain size and velocity components are noted as $L_x$, $L_y$, $L_z$ and $u$, $v$, $w$ in the streamwise $x$, wall-normal $y$, and spanwise $z$ directions, respectively. The bulk Reynolds number is defined for pCf by $\mathrm{Re}_b = \frac{U_w h}{\nu}$ where $h$ is half of the Couette gap width while the bulk flow has a zero mean velocity. The domain used for the simulations has the size of the minimal flow unit (or simply Miniunit) as introduced by Jiménez and Moin [28] and Hamilton *et al.* [24]. Table I shows the mesh grid size used for the simulation of the Miniunit, from some selected publications. Three to four grid points inside the laminar sublayer ($y^+ < 5$) are required in order to calculate accurately the near-wall flow structures.

TABLE I. Simulation domain characteristics for the Miniunit in (a) some selected references and (b) the present work. Mesh is stretched in the $y$ direction and follows an error function mapping $y(k) = \mathrm{erf}(\alpha k)/\mathrm{erf}(\alpha), k = (-1{:}2/N_y{:}1)$ with $\alpha = 2.0$.

(a) In the references

| $\mathrm{Re}_b$ | $\triangle y^+$ | $\triangle x^+$ | $\triangle z^+$ | Reference |
|---|---|---|---|---|
| 4500 | 0.92 (wall)–5.9 (center) | 13.7 | 6.18 | Ref. [2] |
| 3000 | 0.08 (wall) | 7.55 | 4.8 | Ref. [50] |
| 2150 | 0.18 (wall)–8.34 (center) | 12.05 | 6.02 | Ref. [65] |
| 625 | 0.18 (wall)–3.7 (center) | 13 | 8.9 | Ref. [24] |

(b) In the present work

| Case | $\mathrm{Re}_b$ | $L_x \times L_y \times L_z$ | $N_x \times N_y \times N_z$ |
|---|---|---|---|
| | | Stretched mesh | |
| *A* | 500 | $2.75 \times 1.0 \times 1.88$ | $30 \times 86 \times 32$ |
| | | $\triangle y^+_{\min} = 0.08, \triangle y^+_{\max} = 1.91; \triangle x^+ = 7.35; \triangle z^+ = 4.70$ | |
| | | Regular mesh | |
| *B* | 500 | $2.758 \times 1.0 \times 1.939$ | $182 \times 66 \times 128$ |
| | | $\triangle y^+ = \triangle x^+ = \triangle z^+ = 1.19$ | |
| *C* | 500 | $2.758 \times 1.0 \times 1.939$ | $382 \times 134 \times 256$ |
| | | $\triangle y^+ = \triangle x^+ = \triangle z^+ = 0.60$ | |

First simulations of single-phase flow in a Couette configuration were intended to test the unsteady development of the fluid flow initially at rest towards a linear flow when the walls of the domain start to move, at $t = 0$ with velocity $+U_w$ and $-U_w$. The theoretical evolution of the flow profile given by Batchelor [5] occurs with a characteristic diffusion time scale $h^2/\nu$. Figure 6 shows the

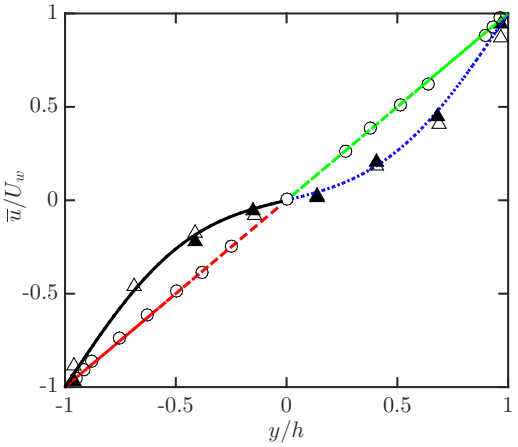


FIG. 6. Streamwise velocity profile in the wall-normal direction starting from fluid at rest. Lines correspond to our simulations: ..... $\mathrm{Re}_b = 365$, $\eta = 0.1$; ——— $\mathrm{Re}_b = 650$, $\eta = 0.1$; - - - $\mathrm{Re}_b = 300$, $\eta = 1.0$; -.-.- $\mathrm{Re}_b = 345$, $\eta = 1.0$, where $\eta$ is the dimensionless time scaled with $h^2/\nu$. Symbols stand for experimental or direct numerical simulation results. △ Tillmark and Alfredsson [64], $\mathrm{Re}_b = 365$, $\eta = 0.1$; ▲ Tillmark and Alfredsson [64], $\mathrm{Re}_b = 650$, $\eta = 0.1$; ○ Reichardt [52], $\mathrm{Re}_b = 300$ when flow is fully developed; • Tillmark and Alfredsson [64], $\mathrm{Re}_b = 345$ when flow is fully developed.

TABLE II. Parameters used in numerical simulations. The particle Reynolds number $\mathrm{Re}_p \equiv \Gamma a^2/\nu$ based on local shear rate $\Gamma = |\frac{du}{dy}|$, and the Stokes number $\mathrm{St} \equiv \rho_p/(3\rho_f)\mathrm{Re}_p$ cancel at the Couette center and are maximum at the wall $\mathrm{Re}_p$(max) takes place near the Couette wall where the shear rate is the strongest.

| Domain size | $L_x \times L_y \times L_z = 0.88\pi \times 1.0 \times 0.6\pi$ | | |
|---|---|---|---|
| $\mathrm{Re}_b$ | 500 | 750 | 1000 |
| $\mathrm{Re}_\tau$ | 39.5 | 52.2 | 67.3 |
| $y^+$ | [0–80.5] | [0–105.4] | [0–134.5] |
| $L_y/d$ | 10, 20 | 20 | 20 |
| $d^+$ | 8.0, 4.0 | 5.3 | 6.7 |
| $\mathrm{Re}_p$(max) | 17.5, 4.38 | 5.83 | 8.75 |
| St(max) | 3.89, 0.97 | 1.30 | 1.94 |
| $\tau_p^+$ | 5.31, 1.37 | 2.32 | 3.77 |
| $\mathrm{St}_{\mathrm{turb}}$ | 0.066, 0.017 | 0.022 | 0.028 |
| Mesh grid | $182 \times 66 \times 128$ (for $L_y/d = 10$) | | $382 \times 134 \times 256$ (for $L_y/d = 20$) |
| $\Phi(\%)$ | | [0, 1, 5, 10] | |

numerical simulation by using case A compared with experiments [52,64]. The numerical code used for this study captures accurately the transient evolution of the streamwise velocity.

Simulations of single-phase turbulent flow were realized in domains needed later for particle-laden flows, with the constraint of three to four grid points per particle radius that must be respected for FCM. Therefore two simulation domains (cases B and C) with regular mesh grids were designed for two Couette gap-to-particle size ratios $L_y/d = 10$ and $L_y/d = 20$. Simulations of single-phase flow in these domains are compared with the simulation based on stretched mesh grid (case A). In cases B and C, at least three points stand inside the laminar sublayer for $\mathrm{Re}_b = 500$. At this Reynolds number, the discrepancy of the mean and rms velocity profiles between simulations using domains A, B, and C is less than 5%.

We also performed simulations of turbulent Couette flow with larger domains in both streamwise and spanwise directions and the comparison with existing experimental data and numerical results from Refs. [6,31,65]. The major effects of increasing the domain size are the following. First, the average velocity gradient is steeper near the walls in larger domains. The nondimensional velocity gradient in the Couette gap near midplane is $\psi = \frac{h}{U_w}\frac{d\tilde{u}}{dy}\,|_{y=0} \approx 0.18$–$0.2$ in large domains (at low $\mathrm{Re}_b$ like in Ref. [65]), whereas it is almost zero in the Miniunit. According to Ref. [65], the nonzero velocity gradient will lead to a finite production of TKE in the midplane. Second, it is found that the streamwise rms velocity is larger, whereas the wall-normal and spanwise components are smaller in the Miniunit compared to larger domains. However, the turbulent Reynolds stress is nearly unchanged close to the boundary, whereas it is slightly smaller in the core region for larger domain size.

Despite these differences, certainly due to the confinement of large-scale vortices in the streamwise direction, the Miniunit is useful because it allows to accommodate a single set of (periodic array of) vortical structures, which are sufficient to reproduce low-order turbulence statistics. In this domain, the turbulence is sustained while the Reynolds number is decreased down to $\mathrm{Re}_b = 330$, below which the flow becomes fully laminar. This threshold for flow relaminarization is slightly higher than in larger simulation domains ($\mathrm{Re}_c = 324 \pm 1$ in Ref. [17]) which accommodate many longer large-scale structures.

## IV. TURBULENT PCF LADEN WITH NEUTRALLY BUOYANT PARTICLES

The dimensionless length and velocity wall units are $y^+ \equiv \frac{yu_\tau}{\nu}$, and $u^+ \equiv \frac{u}{u_\tau}$, where $u_\tau = \sqrt{\frac{\tau_w}{\rho}}$ is the friction velocity based on the wall shear stress. Table II contains a summary of all parameters

selected for this study. Both bulk and frictional Reynolds numbers $\mathrm{Re}_b$ and $\mathrm{Re}_\tau$ are based on the fluid viscosity. The effective Reynolds number $\mathrm{Re}_s$ of the suspension flow is lower than $\mathrm{Re}_b$ due to the increase of energy dissipation by rigid particles in shear flow and depends on the particle concentration $\varphi$. Simulations of suspension flows were performed with two particle sizes $L_y/d = 10$ and 20 and at $\mathrm{Re}_s$ larger than the laminar-turbulent transition threshold. Since one cannot be sure *a priori* that the suspension will behave like an effective fluid with equivalent properties, we verified *a posteriori* the flow turbulent nature and statistics. Most of the two-phase flow simulations were carried out at a Reynolds number $\mathrm{Re}_b = 500$ and were compared to a reference effective fluid flow, at mixture Reynolds number equal to $\mathrm{Re}_s = \frac{U_w h}{\nu_{\mathrm{eff}}}$. The effective viscosity $\nu_{\mathrm{eff}}$ was estimated from an Eilers fit for low Reynolds number suspensions and *a posteriori* compared to the real suspension viscosity obtained from the shear stress distribution as explained further in this section:

$$\nu_{\mathrm{eff}} = \nu\left[1 + \frac{1.25\Phi}{1 - \Phi/0.63}\right]^2.$$

In the turbulent flow, particles experience turbulent forcing with a characteristic time scale $\tau_f^+ \sim L_y^+/\max(v'^+|w'^+)$ related to large-scale vortices. The characteristic time scale for a particle to relax when submitted to flow forcing is given by

$$\tau_p^+ = \frac{2}{9}\left(\frac{\rho_p}{\rho_f} + \frac{1}{2}\right)\mathrm{Re}_\tau^2\left(\frac{d}{L_y}\right)^2. \tag{12}$$

The ratio of particle to fluid time scales leads to the definition of a Stokes number $\mathrm{St}_{\mathrm{turb}} = \tau_p^+/\tau_f^+$ related to the flow turbulence. Referring to the test of one particle oscillating in a steady fluid, this Stokes number can be related to the dimensionless Stokes layer by $\delta^2 = 9\pi/(\rho_p/\rho_f + 1/2)\mathrm{St}_{\mathrm{turb}}$. $\delta^2$ is below 0.5 for $L_y/d = 20$ and reaches its maximum value $\delta^2_{\max} = 1.25$ for $L_y/d = 10$. Therefore the turbulent flow simulations considered for this paper are within the range of validity of FCM. The statistics were performed using ensemble averages over 500 time units (time unit is $h/U_w$).

### A. Velocity profiles

In turbulent single-phase pCf, mean velocity profile is governed by streamwise vortices. The suspension flow profile is very close to single-phase configuration as observed in Fig. 7. The largest discrepancy occurs at the highest concentration $\Phi = 10\%$ for the highest Reynolds number, $\mathrm{Re}_b = 1000$. Since the mean velocity profile is mainly governed by large-scale vortices [24], i.e., here the vortex pair, we can conclude that particles did not modify significantly the large scales.

The evolution in time of the total friction coefficient is displayed in Fig. 8. The friction coefficient is calculated from the sum of shear stress on both walls $[C_f = 2\tau_w/(\rho U_w^2)]$. Both single-phase and particle-laden flows with $\Phi = 10\%$ are shown. The suspension wall shear stress is slightly larger than for single phase. Consequently the power input from the moving walls per unit time $[\int_0^{L_z}\int_0^{L_x} U_w\tau_w(x,z)\,dx\,dz]$ is larger for suspension flows. This observation is almost independent of the Reynolds number and particle size. In Fig. 8 the amplitude and frequency of wall friction fluctuations are modified by the presence of particles. It is a first indication that the flow intermittency is altered by particles.

### B. Spatial distribution of particles

Figure 9 shows the concentration profiles for different $\mathrm{Re}_b$, particle sizes, and bulk concentrations. In all cases, the concentration is higher in the core than near the walls, due to particle inertial migration as explained in Sec. II. The profiles of concentration are the result of an equilibrium between several mechanisms. On the one hand the hydrodynamic wall repulsion and turbulent ejection events push the neutrally buoyant particles towards the center of the gap, whereas on the other hand, turbulent sweep events pull the particles towards the walls. Although on average the concentration profiles

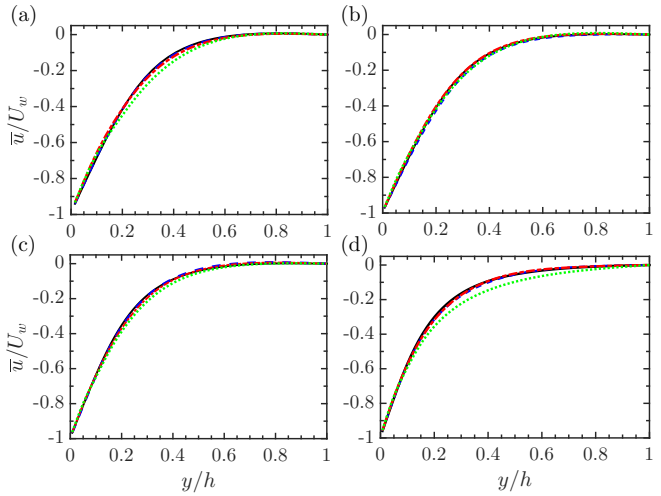


FIG. 7. Mean velocity profiles for different Reynolds numbers, particle sizes, and bulk concentrations. (a) $\mathrm{Re}_b = 500$, $L_y/d = 10$; (b) $\mathrm{Re}_b = 500$, $L_y/d = 20$; (c) $\mathrm{Re}_b = 750$, $L_y/d = 20$; (d) $\mathrm{Re}_b = 1000$, $L_y/d = 20$. The lines stand for different solid concentration: —— $\Phi = 0\%$; – – – $\Phi = 1\%$; -·-·- $\Phi = 5\%$; ····· $\Phi = 10\%$. The profiles are symmetric with respect to the Couette center plane. Therefore half of all the profiles are shown between $y = 0$ (wall) and $y = h$ (center) in this figure and elsewhere.

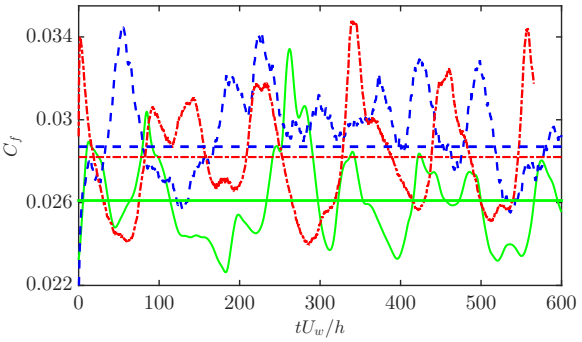


FIG. 8. Temporal evolution of the wall friction coefficient ($C_f$, summed on both walls) at $\mathrm{Re}_b = 500$. —— single-phase flow; – – – $L_y/d = 10$, $\Phi = 10\%$; -·-·- $L_y/d = 20$, $\Phi = 10\%$. Straight lines stand for temporal averages.

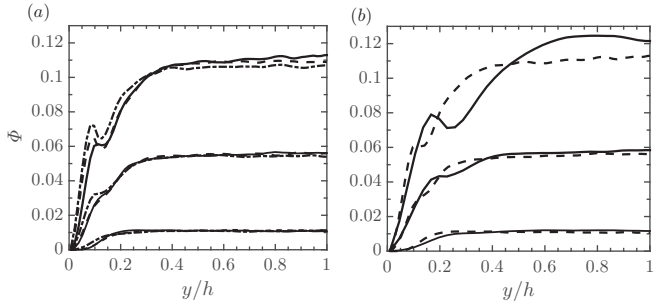


FIG. 9. Concentration profiles for different Reynolds numbers, particle sizes, and bulk concentrations. From bottom to top $\Phi$: 1,5, and 10%. (a) $L_y/d = 20$ and ——$\mathrm{Re}_b = 500$; – – – $\mathrm{Re}_b = 750$; -·-·- $\mathrm{Re}_b = 1000$. (b) $\mathrm{Re}_b = 500$ and —— $L_y/d = 10$; – – – $L_y/d = 20$.

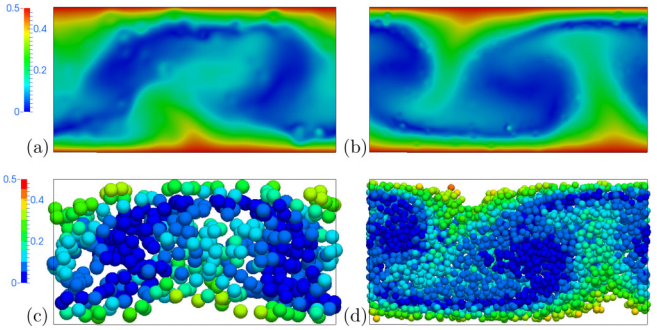


FIG. 10. Top panels: contours of the magnitude of the streamwise flow velocity in the middle cross section. Bottom panels: particle positions projected on the plane $(y,z)$, colored according to local magnitude of streamwise velocity. Comparison between $L_y/d = 10$ (left) and 20 (right) for $\mathrm{Re}_b = 500$ and $\Phi = 5\%$.

are relatively flat, snapshots in the wall normal-spanwise plane show strong instantaneous coupling between the spatial distribution of neutrally buoyant particles and flow structures as noted in Fig. 10.

A local maximum can be noticed in the concentration profile near the walls. It is more evident at higher average concentrations ($\Phi = 5$ and 10%) and higher $\mathrm{Re}_b$. Picano *et al.* [49] noted that these peaks are of the same order of magnitude as the bulk concentration, and therefore they are not related to turbophoresis drift typically observed in dilute suspensions when particles are heavier than the fluid. These near-wall layers are the result of excluded volume effects when particles are gathering in the near wall region.

### C. Turbulence intensity

Figure 11 shows the normal Reynolds stress components of turbulence agitation for two-phase flows which are compared to single-phase configurations. They are all scaled with $u_\tau$, the friction velocity of single-phase flow at the corresponding Reynolds number $\mathrm{Re}_b$. The overall turbulent intensity is not much modulated by particles. Close to the walls ($y^+ < 20$), $u'_{\mathrm{rms}}$ slightly decreases, whereas transverse components increase with concentration, especially the wall-normal component $v'_{\mathrm{rms}}$. The increase of transverse velocity fluctuations with concentration is even more pronounced with larger particles. It is not necessarily due to the increase of turbulent activity but more likely related to the local peak of concentration observed near the wall (at $y^+ = 8 - 10$ when $\mathrm{Re}_b = 500$) where shear is large and generates frequent particle encounters.

Also velocity fluctuations profiles in all directions are flatter for particle-laden than single-phase flow. This indicates that particles redistribute the fluctuating energy into a more isotropic flow. The trend towards isotropy is more pronounced with larger particles. Such a trend was also observed in pressure-driven flows [49] with neutrally buoyant finite-size particles, whereas it is noticeably different for inertial point particles [54].

### D. Energy spectrum

Wall-normal profiles of turbulence intensity did not show significant modification of turbulence features in the Couette flow. These profiles are mainly dominated by large-scale vortices which do not seem to be influenced by the presence of particles (Fig. 11). The size of particles being between the largest and smallest length scales, it is interesting to investigate the influence of particles' energy distribution among various scales of the flow.

Fourier transform of the turbulent kinetic energy (TKE) is calculated in order to analyze the energy cascade. Figure 12 shows the average Fourier transform of the streamwise velocity fluctuations $E^{\Phi}_{uu}$ scaled by $U_w^2$ as a function of the streamwise wave number scaled by the inverse of both viscous

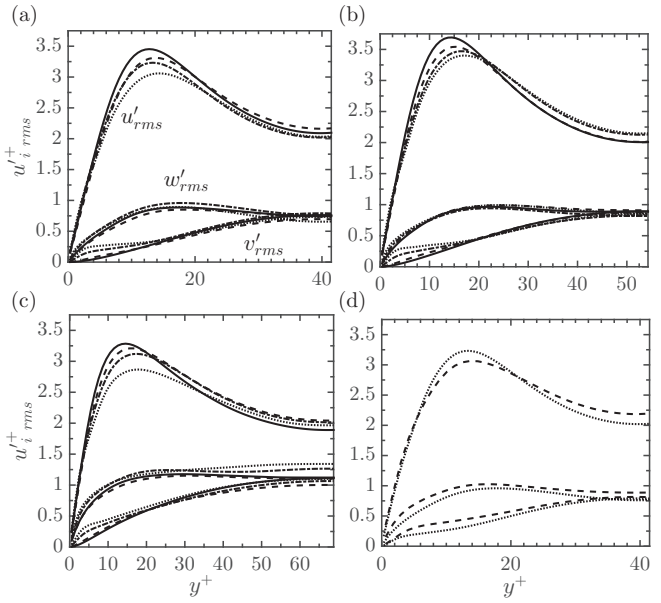


FIG. 11. Profiles of velocity rms for different Reynolds numbers, particle sizes and bulk concentrations. (a) $\mathrm{Re}_b = 500$, $L_y/d = 20$; (b) $\mathrm{Re}_b = 750$, $L_y/d = 20$; (c) $\mathrm{Re}_b = 1000$, $L_y/d = 20$; (d) $\mathrm{Re}_b = 500$, $\Phi = 5\%$. Half of the domain is shown because of midplane symmetry. From (a) to (c): ____ $\Phi = 0$; _ _ _ $\Phi = 1\%$; _ . _ . $\Phi = 5\%$; ..... $\Phi = 10\%$. (d) _ _ _ $L_y/d = 10$; ..... $L_y/d = 20$.

length scale and particle size. The single-phase flow spectra are calculated with a stretched mesh (finer in the viscous sublayer) and regular mesh. The wave number is scaled by the viscous length scale wave number. Both single-phase spectra are close, indicating that the near wall turbulent structures are well captured by the regular mesh. The maximum energy is contained in the largest wavelength corresponding to the domain size in the streamwise direction, because large-scale rolls fill the entire domain length in the minimal unit. The energy drops considerably at wavelengths between half and quarter of the Couette gap size. The energy spectra of single-phase flow are

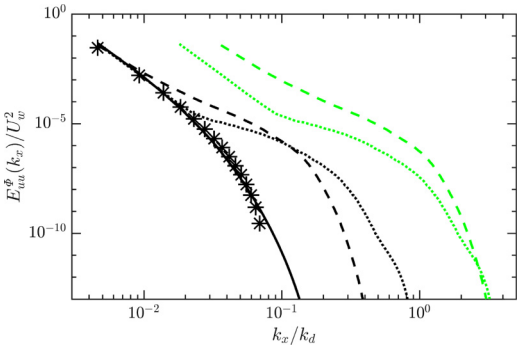


FIG. 12. TKE spectra as a function of wave number in streamwise direction. Single phase of $\mathrm{Re}_b = 500$ scaled by $k_d = 2\pi/\delta_v$: $*$ stretched mesh; ____ regular mesh for $L_y/d = 20$. Two-phase flow with $\Phi = 10\%$ and $\mathrm{Re}_b = 500$ for two particle sizes: _ _ _ $L_y/d = 10$ and ..... $L_y/d = 20$, scaled by $k_d = 2\pi/\delta_v$; _ _ _ $L_y/d = 10$, scaled by $k_d = 2\pi/d_{10}$; ..... $L_y/d = 20$, scaled by $k_d = 2\pi/d_{20}$. $d_{10}$ and $d_{20}$ correspond to particle diameter, and $\delta_v$ is the viscous length scale based on single-phase flow.

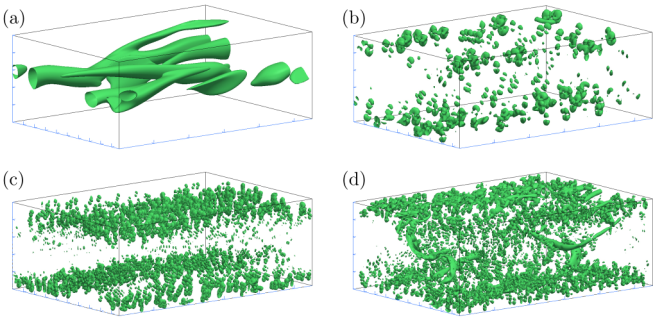


FIG. 13. Vortex identification for single-phase flow and two-phase flows using $\lambda_2$ criterion. (a) single-phase flow with $\mathrm{Re}_b = 500$ using $\lambda_2 = -0.1$; $\Phi = 5\%$ and $\lambda_2 = -1.0$ for the followings. (b) $L_y/d = 10$ and $\mathrm{Re}_b = 500$; (c) $L_y/d = 20$ and $\mathrm{Re}_b = 500$; (d) $L_y/d = 20$ and $\mathrm{Re}_b = 1000$.

compared to the two-phase dispersed flows for both particle sizes with an unique scaling of the wave numbers by the same $2\pi/\delta_\nu$ based on single-phase flow, all spectra matched at small wave numbers, indicating that the large-scale motions were not modified by the presence of the particles. The energy is increased at the smallest scales because finite-size particles induce perturbations and small-scale vortices near the particle surface especially in the high-flow shear rate regions. This unified scaling shows in addition that the deviation from the single-phase flow spectrum is correlated with the actual size of the particles, as this deviation takes place at smaller wave numbers for the largest particles we investigated. The energy spectra plotted for different particle sizes overlap with each other at large wave numbers, if they are scaled by the respective particle size.

This suggests that finite-size particles promote continuous energy transfer across all scales in the turbulent Couette flow. Actually, finite-size particles add perturbation to the sheared or strained flow, as displayed in Fig. 13 using the $\lambda_2$ criterion. The number of small-scale vortices is increased due to local distortion of flow vortices by particles, similarly to what was described in the experiment of Tanaka and Eaton [63] who measured the flow around a single particle. These perturbations induced by finite-size particles make turbulence in suspension flow more isotropic.

### E. Shear stress budget

The streamwise momentum balance of the suspension flow in a Couette geometry yields a constant shear stress $\tau_{\mathrm{total}}$ across the gap. In single-phase flow, the shear stress is composed of two contributions, namely, viscous and Reynolds stress contributions. In particle-laden flow, additional momentum transfer arises due to particle rigidity, to the forces and torques they apply on the fluid, and to their fluctuating motion with respect to local flow. The decomposition of the shear stress according to Batchelor is given in Appendix B. The increase of stress due to particle rigidity $\tau_s$ is calculated using the particle-induced stresslet (from the dipole tensors associated to each particle) as follows:

$$\tau_s(y) = \frac{1}{TL_xL_z}\int_0^T\int_0^{L_z}\int_0^{L_x} dG_{ij}(x,y,z,t)\,dx\,dz\,dt. \tag{13}$$

The integral over the streamwise and spanwise directions is calculated in slabs of width $dy$, and the differential $dG_{ij}$ refers to weighting the stresslet by the percentage of particle volume included into a slab. From $\tau_s(y)$ one can calculate the increase of mixture viscosity using

$$\frac{\nu_{\mathrm{eff}}(y)-\nu}{\nu} = \frac{\tau_s(y)}{\nu\Gamma(y)}, \tag{14}$$

where $\nu_{\mathrm{eff}}$ is the effective suspension viscosity taking into account the presence of particles. It depends on the wall-normal position because the stresslet terms depend on local shear rate. Figure 14

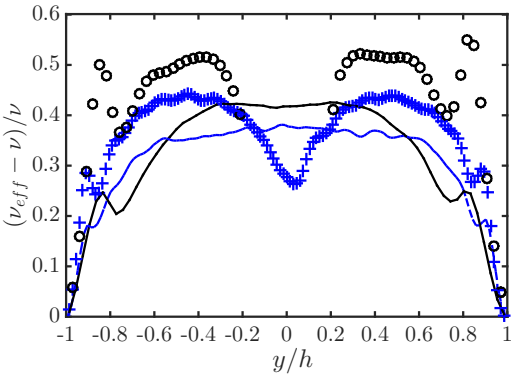


FIG. 14. Profiles of relative mixture viscosity across the Couette gap for $\mathrm{Re}_b = 500$, $\Phi = 10\%$ and two particle sizes $L_y/d = 10{,}20$. Eilers fit $([1 + 1.25\Phi/(1 - \Phi/0.63)]^2 - 1.0)$ based on the local concentration $[\Phi(y/h)]$ for two particle sizes: —— $L_y/d = 10$; - - - $L_y/d = 20$; Eq. (14) based on the local shear stress: ○ $L_y/d = 10$; + $L_y/d = 20$.

displays the effective viscosity profiles for two particle sizes. They are compared to the Eilers fit (low Reynolds limit) based on the local concentration of particles. As expected from the studies on the effect of finite particle Reynolds number on suspension viscosity [33,62,69], the suspension viscosity increases [as $O(\mathrm{Re}_p^{3/2})$ in the dilute limit]. The ratio of the average effective viscosity in the present simulations and that of Eilers fit is 1.11 for $L_y/d = 10$ and 1.02 for $L_y/d = 20$. Note that the decrease of effective viscosity near the midplane is due to local weak shear rates.

Figure 15 shows the dependence on bulk concentration of all terms in Eq. (B4), for different Reynolds numbers and particle sizes. Our numerical simulations lead to an accurate balance for the shear stress. Only a slight imbalance is obtained near the wall or in the core region at the highest concentration where the residual is ±3%. Particle size (up to $L_y/d = 10$ used in this work) has no significant effect on the shear stress budget contributions.

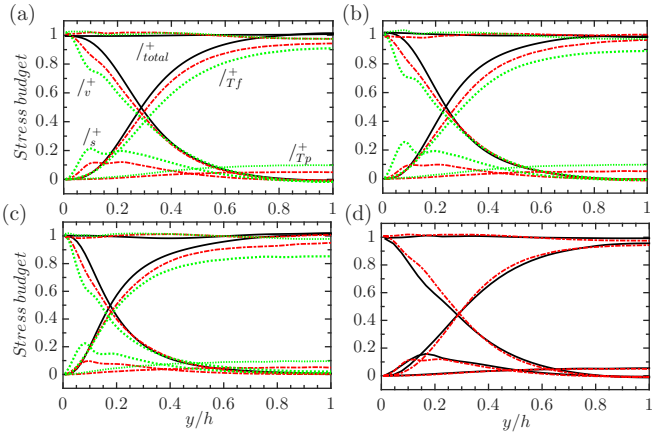


FIG. 15. Profiles of the shear stress budget components for different Reynolds numbers, particle sizes, and bulk concentrations. Plots in (a) to (c) compare single-phase flow results (solid line) to two-phase flow simulations (dashed lines) at - - - $\Phi = 5\%$ and ····· $\Phi = 10\%$. In (d) the shear stress components are compared at $\Phi = 5\%$ —— $L_y/d = 10$ and -·-·- $L_y/d = 20$.

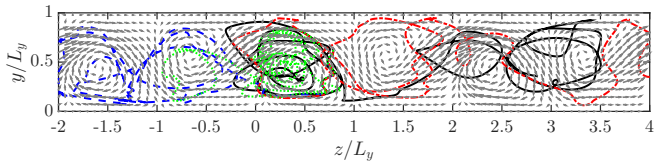


FIG. 16. Effect of particle inertia on the trajectory of a single particle in turbulent pCf at $\mathrm{Re}_b = 500$. ..... bubble; $\rho_p/\rho_f = 1.0$; -.-.- $\rho_p/\rho_f = 2.0$; - - - $\rho_p/\rho_f = 5.0$.

The impact of increasing the bulk concentration on stress components depends on the wall-normal distance. The fluid and particle turbulent stress contributions reach their maximum values at the gap center, where cross-gradient mixing (as defined in Ref. [56]) is ensured by large-scale structure motion [35]. When concentration increases, turbulent fluid stress is reduced, whereas turbulent particle stress is enhanced. Near the walls, the momentum transfer is governed by the viscous contribution. When the concentration increases, the fluid viscous stress decreases, whereas the rigidity stress significantly increases (it becomes as high as 20% of the total stress), the latter being especially promoted by the high shear rate of the flow near the walls (whereas it is almost zero at the center of the gap).

## V. EFFECT OF INERTIAL PARTICLES AND BUBBLES

Before studying the influence of particle density on the turbulent flow statistics, we considered the trajectory of a single particle in turbulent pCf in order to observe if it exhibits preferential position depending on its inertia, like in Taylor-Green vortex (see Appendix A). Figure 16 shows the particle trajectory with unfolded periodic boundary conditions. Like in a Taylor-Green vortex, the lighter particle $\rho_p/\rho_f = 1.2.10^{-3}$ is trapped inside one of the large-scale vortices and can hardly leave it. The neutrally buoyant particle spans the entire domain. Heavier particles $\rho_p/\rho_f = 2.0{,}5.0$ tend slightly to be ejected out of LSVs in the high-speed streak where the fluid is swept towards the wall. These observations suggest that the concentration spatial distribution for two-phase flow laden with denser or lighter particles might be different from the case with neutrally buoyant particles.

Simulations of suspensions with light ($\rho_p/\rho_f = 1.2.10^{-3}$) and heavy ($\rho_p/\rho_f = 2.0{,}5.0$) particles are realized with the small particle size, i.e., $L_y/d = 20$ for flow Reynolds number $\mathrm{Re}_b = 500$ and concentration $\overline{\Phi} = 10\%$. The Stokes number corresponding to the these density ratios range from 0.0012 to 4.85.

The average concentration contours in the transverse plane is shown in Fig. 17. These contours are averaged over $\sim$400 time units. As it can be expected, bubble concentration is higher inside the

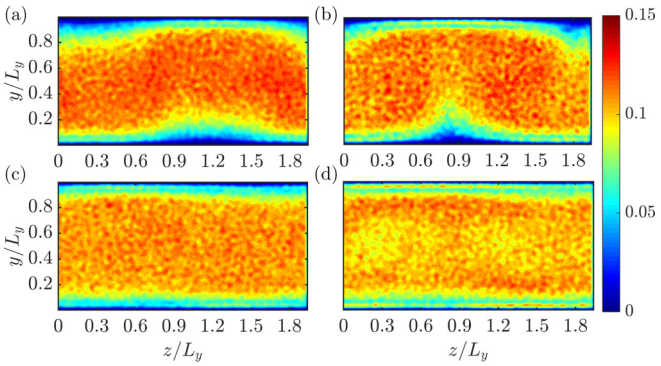


FIG. 17. Contour of particle concentration in the transverse $y$-$z$ plane averaged over $\sim$400 time units. (a) Bubble; (b) $\rho_p/\rho_f = 1.0$; (c) $\rho_p/\rho_f = 2.0$; (d) $\rho_p/\rho_f = 5.0$.

core of the flow. Bubbles are not exclusively found inside the vortex cores: they are permanently exchanged between both rolls. For denser particles, the probability of finding them close to the Couette walls increases with the density. Unlike neutrally buoyant particles, they are found in both low- and high-speed streaks (ejection regions). The preferential accumulation found for these finite-size particles correspond to a distance equal to one particle radius from the wall [see 18(b) It is different from what is known on heavy point particles that tend to "stick" near the walls in pCf; see, for instance, Richter and Sullivan [54]. This phenomenon, called turbophoretic drift, has been already observed in the experiments of Ref. [71], which investigated the interaction between turbulent-burst activity and deposited particles within the viscous sublayer. They suggested that, once particles of diameter less than 1.3 viscous sublayer thickness are trapped in this layer, wall normal flow velocity fluctuations are not efficient anymore for particle re-entrainment in the bulk.

The velocity profiles of pCf laden with light and heavy particles are plotted in 18(a). They are similar to the profiles obtained with neutrally buoyant particles. As discussed earlier in this paper, the mean velocity profile is governed by LSVs in turbulent pCf, which seem to be unaffected by the particle distribution at the average solid volume fraction we considered. The inset in this figure displays $\overline{\tau_w}/(\mu U_w/h)$ as a function of the density ratio. The mean wall friction is slightly enhanced when inertia is increased.

Figure 18(c) shows the diagonal components of rms velocity fluctuation tensor scaled by the corresponding wall friction velocity $u_\tau$. Turbulence modulation is observed in Refs. the case $\rho_p/\rho_f = 5$, in contrast with what is classically observed for heavy point particles [16,36]. Point particles add energy dissipation through the drag force in the fluid phase momentum balance. Their slip velocity increases with inertia and damped turbulent fluctuations, especially in transverse directions. In the case of heavy finite-size particles as shown in 18(c), $u'_{\mathrm{rms}}$ decreases across the gap, whereas transverse components are unchanged when the density ratio is increased.

Finally, modification of energy distribution by particles is considered. The question related to the effect of particle inertia on turbulence modulation does not have a unique answer in the literature. Many works were done with very high density ratio (gas-solid), and the conclusions depend upon the flow configuration (see, for example, Refs. [18,53]). Therefore the impact on the flow energy distribution is different when coupling particle finite size with particle fluid density mismatch. The average streamwise energy spectrum $E^{\Phi}_{uu}$ is plotted in 18(d) as a function of both streamwise and spanwise wave numbers, for the cases of light and heavy particles in comparison with the neutrally buoyant case. Inertia does not significantly influences the energy transfer process in the range of parameters we considered.

## VI. MODIFICATION OF THE REGENERATION CYCLE

The shape of LSVs can be clearly observed in Fig. 19(a) that displays the streamwise vorticity. As mentioned before, in Miniunit, two spanwise counter-rotating LSVs are filling the entire simulation domain.

As stated by Waleffe [68] and Hamilton *et al.* [24], turbulence activity in turbulent pCf follows a regeneration cycle with a period of $\sim 100h/U_w$ when $\mathrm{Re}_b = 400$. Each cycle consists of three sequential subprocesses: streak formation, streak breakdown, and vortex regeneration. Streak formation is due to an ejection event by two counter-rotating large-scale vortices, which forms a low-speed streak by pumping fluid away from the no-slip boundary. When a streak comes across the region of strong mean shear flow, streak breakdown occurs forming a secondary flow. Finally the vortex is regenerated due to the breakdown of streaks, being governed by a strong nonlinear process. In this part, we consider large-scale streaks (LSSs) and LSVs separately, in view of understanding how finite-size particles are affecting the regeneration cycle. We will observe that the particles reduce the magnitude of $\omega_x$ only in the core of the LSVs, without changing significantly their shape and size.

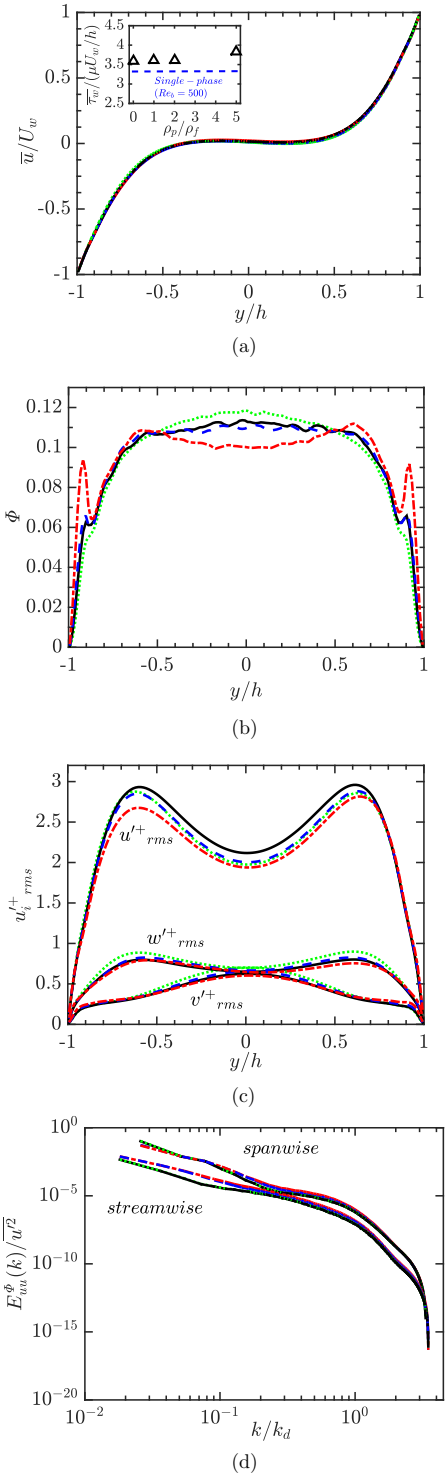


FIG. 18. Effect of inertia on the turbulent flow statistics. Mean profiles of (a) streamwise flow velocity, (b) concentration, and (c) rms of velocity fluctuations. (d) Contains TKE spectrum as a function of streamwise and spanwise wave numbers ($L_y/d_{20} = 20$ and $k_d = 2\pi/d_{20}$). The line style is the same as in Fig. 16.

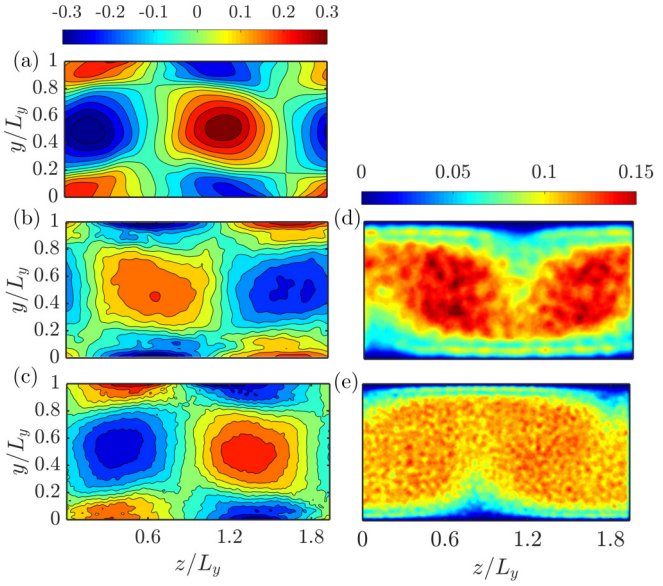


FIG. 19. Streamwise vorticity averaged over ∼500 time units, comparison between (a) $\mathrm{Re}_b = 500$, single-phase flow and (b, c) $\mathrm{Re}_b = 500$, $\Phi = 10\%$ for two particle sizes $L_y/d = 10, 20$, respectively. The corresponding contours of concentration projected onto the transverse plane ($y$-$z$ plane) is shown in (d) and (e).

### A. Quadrant analysis

An LSS corresponds to an ejection or sweep event, that can be identified by sampling $u'$-$v'$ correlation as shown in Fig. 20 (probability distribution is also shown). This figure is realized in the midplane ($xz$) along the wall-normal direction. The LSS are identified from events ($u' < 0, v' > 0$) and ($u' > 0, v' < 0$) in the second and fourth quadrants that are dominant in this plane. In pCf configuration, sweep and ejection events cannot be distinguished because an ejection from one wall which is crossing the midplane corresponds to a sweep on the opposite wall. Figure 20 reports on these events taking place in single-phase flow as well as for two-phase flow with neutrally buoyant particles. The event distribution is stretched from a curved shape to a more straight one, suggesting

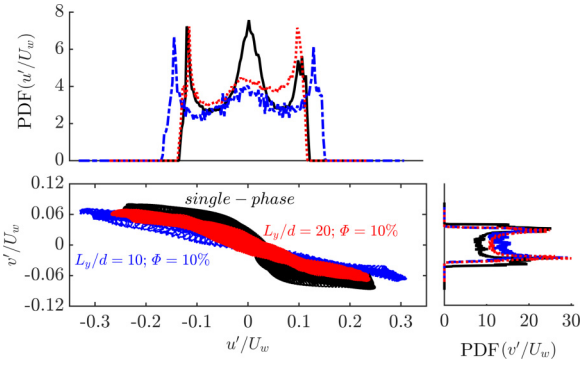


FIG. 20. Modification by the neutrally buoyant particles of the quadrant analysis of $u'$ and $v'$ and of their probability density functions (PDFs) in the Couette center plane. The single-phase plots in solid lines are performed at the effective Reynolds number of the suspension flow ($\mathrm{Re}_s = 380$). Other lines are from two-phase simulations at $\Phi = 10\%$ and $\mathrm{Re}_b = 500$. - - - $L_y/d = 10$; ····· $L_y/d = 20$.

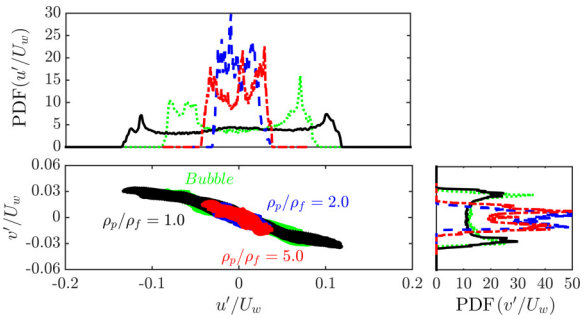


FIG. 21. Effect of particle inertia on the modification of the quadrant analysis of $u'$ and $v'$ and of their PDFs in the Couette center plane, for $L_y/d = 20, \Phi = 10\%$ and $\mathrm{Re}_b = 500$. The line style is the same as Fig. 16.

that the shape of the streak is altered by particles especially for $L_y/d = 10$. The probability density functions of $u'$ and $v'$ reveal that the interaction between particles and streaks promotes strong streamwise fluctuations with no significant impact on wall-normal fluctuations.

Similar analysis is realized with light and heavy finite-size particles. The shape of streak is clearly altered when heavier particles are added to the flow (see Fig. 21). Particularly in the streamwise direction, the intensity of $u'$ is drastically reduced corresponding to the $u'_{\mathrm{rms}}$ attenuation as in Fig. 18(c). In the present study, both lighter and heavier finite-size particles have damped the turbulence intensity in the midplane compared with neutrally buoyant particles. On the other hand, the maximum of $v'$ is decreased due to inertial heavier particles while its rms is almost unchanged as shown in Fig. 18(c).

### B. Modal decomposition of velocity fluctuations

To evidence the energy contained in different flow structures, we performed modal analysis of the flow fluctuating energy. The Fourier decomposition of the energy, as introduced by Hamilton *et al.* [24] in the periodic directions (streamwise and spanwise), is written as

$$M(k_x = m\alpha, k_z = n\beta) \equiv \left\{ \int_0^1 [\widehat{u'}^2(m\alpha, y, n\beta) + \widehat{v'}^2(m\alpha, y, n\beta) + \widehat{w'}^2(m\alpha, y, n\beta)]dy \right\}^{1/2}, \quad (15)$$

where $(m,n)$ are the integer wave numbers, and $(\alpha,\beta)$ are the fundamental wave numbers in streamwise and spanwise directions defined as $(2\pi/L_x, 2\pi/L_z)$. A combination $(m\alpha, n\beta)$ represents different characteristic turbulent structures. For instance, $(0, n\beta), n \neq 0$ is the $x$-independent structure (e.g., LSS) and $(\alpha, n\beta), n \neq 0$ is the $x$-dependent structure (e.g. streaks confined in the streamwise direction).

Figure 22 shows the evolution in time of the finite energy modes, the highest energy content corresponds to the mode $(0,\beta)$. The energy signals are fluctuating in time with a period of order 100 time units, resulting from flow intermittency. In Fig. 22, $M(0,\beta)$ and $M(\alpha,0)$ are plotted for two particle sizes and compared with single-phase flow at $\mathrm{Re}_s = 380$. The average values of $M(0,\beta)$ and $M(\alpha,0)$ are nearly unchanged. However, one can note that the intermittent character of the flow is modified by the particle presence, since the amplitude of fluctuations is reduced, and the period is also modified, especially by the large particles. As a conclusion, particles have an effect on the streaks dynamics. However, this modification is not strong enough to destroy the stability of the cycle sustaining shear-driven turbulence.

Figure 23(a) shows the effect of particle inertia on the time evolution of $M(0,\beta)$ and $M(\alpha,0)$, based on the simulations with small particles ($L_y/d = 20$). In all cases the average energy content is almost unchanged. Inertial particles have the same effect as the neutrally buoyant particles. As

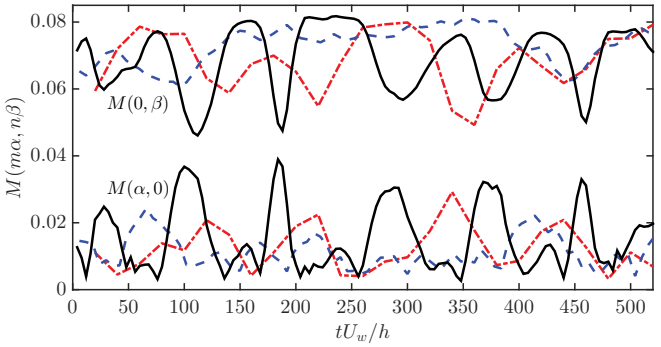


FIG. 22. Modal decomposition: $M(0,\beta)$ and $M(\alpha,0)$. The solid lines are for single-phase flow with effective Reynolds number $\mathrm{Re}_s = 380$; The two-phase flow simulations are obtained for neutrally buoyant particles using $\Phi = 10\%$ and $\mathrm{Re}_b = 500$ and - - - $L_y/d = 10$; ..... $L_y/d = 20$.

for the bubble-laden case, the frequency and amplitude of both modes are very close to single-phase flow configuration, suggesting that bubbles have weak impact on turbulent flow activity.

Hamilton and co-workers [23,24] stipulated that over one cycle, vortices must have a maximum circulation above a given threshold in order to produce unstable streaks so that turbulence can be sustained. We consider the circulation based on the contour that gives the maximum circulation from among all rectangular contours. The circulation of the streamwise vortices of mode 0 in the streamwise direction (like the streaks), and mode $n$ in the $z$ direction is

$$\Gamma_{k_x=0} = \int \hat{\omega}_x(0,y,n\beta)d\mathbf{S}(\mathbf{n}), \tag{16}$$

where $\mathbf{S}(\mathbf{n})$ is a transverse surface, with $y$ varies from 0 to 1 and $z$ varies from 0 to $2\pi/(n\beta)$ for $n \neq 0$. The maximum circulation corresponds to $n = 1$.

Figure 23(b) shows that, regardless of particle inertia, the dimensionless circulation $\Gamma_{k_x=0}/4U_w h$ is higher than the threshold given by Ref. [24], which is 0.0375. Like the modal energy, the average value of the circulation is maintained, whereas the amplitude of fluctuations around the mean is reduced when particle inertia is increased. We can note that the circulation oscillation has phase shift when compared to $M(0,\beta)$ (standing for LSS) in Fig. 23(a). The circulation is the highest when the energy of the streaks is the lowest. It can be noted that the flow circulation is in phase with the $x$-dependent streamwise streaks in Figs. 23(a) and 23(b). Hamilton *et al.* [24] argued that generation of LSSs is the result of nonlinear interactions of $x$-dependent streaks. These $x$-dependent streaks are part of the coherent structures that are the constitutive elements of near-wall turbulence, and they are closely linked to the vorticity stretching ($\omega_x \partial u/\partial x$, where $\omega_x$ is the streamwise vorticity) as demonstrated by Schoppa and Hussain [60]. Instantaneous snapshots containing contours of both the streamwise velocity fluctuations (that illustrate the streak shape), as well as the vorticity stretching term are displayed in Fig. 24. This figure shows that the high-flow circulation is synchronized with the appearance of $x$-dependent flow structures. This gives a strong proof that nonlinear processes like streak breakdown, and thereby vortex regeneration, take place in the considered suspension flows like in single-phase flow, regardless of particle inertia.

### C. Evolution of Reynolds stress

In turbulent wall shear flows, ejection events are driven by the presence of coherent structures such as hairpin vortices or LSVs. Ejections of fluid and sweeps are always responsible for energy transfer from large-scale flow structures in the bulk to small-scale near-wall structures. During this process, the turbulent fluctuations are enhanced. From the investigation of total energy input and dissipation rate, Kawahara and Kida [29] evidenced the temporal evolution of spatial structures. They observed

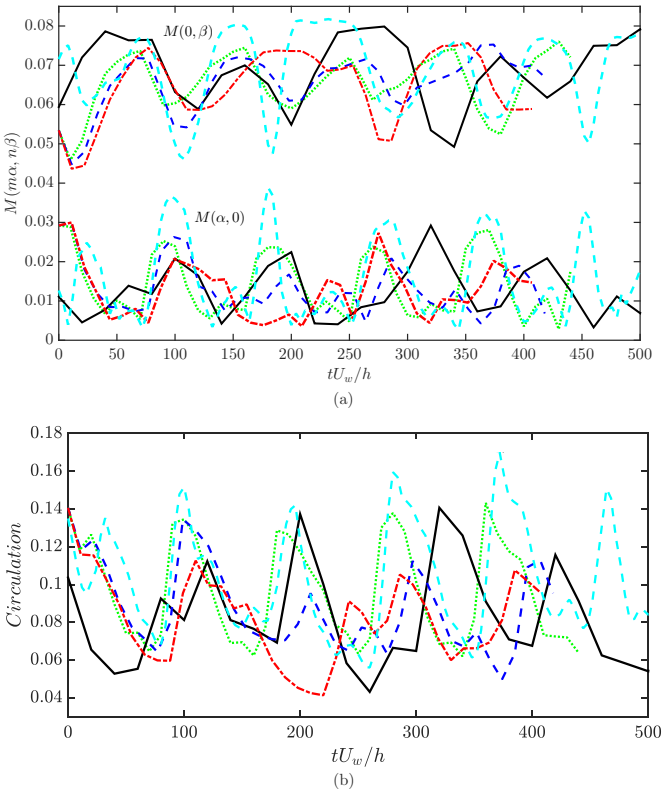


FIG. 23. Effect of inertia on (a) modal decomposition and (b) flow circulation. The light blue dashed line is for single-phase flow with effective Reynolds number $\mathrm{Re}_s = 380$. Other lines correspond to two-phase flow simulations with $\mathrm{Re}_b = 500$ and smaller particles $L_y/d = 20$. with ····· bubble; —— $\rho_p/\rho_f = 1.0$; – – – $\rho_p/\rho_f = 2.0$; –·–·– $\rho_p/\rho_f = 5.0$.

that this cyclic sequence is consistent with the regeneration cycle proposed by Hamilton *et al.* [24]. This quasiperiodicity of the ejection events can be represented by the evolution of Reynolds stress in Fig. 25. We can observe that the maximum of Reynolds stress amplitude occurs in the core region rather than at the walls. The quasiperiodic evolution of Reynolds stress is existing for all single-phase and two-phase configurations. A strong ejection event is followed by a gradual decrease of intensity over a certain time period. The maxima of the temporal evolution of the Reynolds stress occur when dissipation rate is large along the periodic orbit described in Ref. [29]. This maximum intensity of ejection event is decreasing with heavy particles corresponding to a reduction of the level of turbulent fluctuations as shown in 18(C). The typical period of ejection events occurrence is longer when $\mathrm{Re}_b$ is lower [see Figs. 25(a) and 25(b)]. Moreover, this time interval between strong ejection for particulate flows [Figs. 25(c)–25(f)] becomes very similar to single-phase flow associated to effective viscosity [Fig. 25(b)] highlighting that enhanced dissipation by the presence of particles is a major effect on the flow. Either larger particle size or higher particle density has a tendency to delay ejection events compared to single-phase flows.

It is interesting to compare this evolution to the minimal turbulent channel flow investigated in Ref. [26]. Although both of them are wall shear turbulence, the configurations of channel flow and pCf lead to different flow dynamics of ejection events due to the interaction between high- and low-speed streaks. As stated by Itano and Toh [26], two walls share one buffer layer and a couple of LSVs in pCf whereas the channel flow contains log-law region and the central region is ruled by the

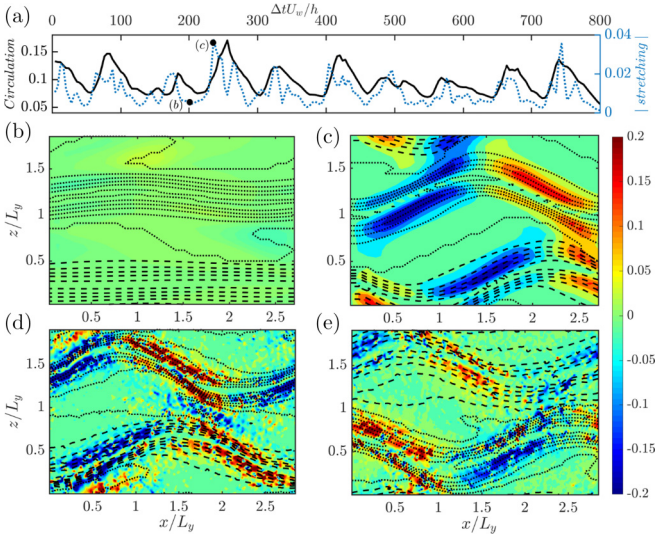


FIG. 24. (a) Time evolution of —— Circulation and ..... spacial average of the absolute value of vorticity stretching ($|\ \omega_x \partial u/\partial x\ |$ within $0.2 < y/L_y < 0.8$ where LSVs take place as seen in Fig. 19) in single-phase flow and $\mathrm{Re}_b = 380$. (b)–(e) Contours of the streamwise velocity fluctuations $u'/U_w$ in the Couette central plane ($y/L_y = 0.5$), showing the streak structures. The iso-contour interval is 0.07. ..... stands for $u'/U_w < 0$ and – – – stands for $u'/U_w > 0$. The color contours indicate the stretching term $\omega_x \partial u/\partial x$. (a) and (b) are for single-phase flow and $\mathrm{Re}_b = 380$, with $x$-independent flow (at the trough of the vorticity stretching instant $\Delta tU_w/h = 200$) and for $x$-dependent flow (at the peak of the vorticity stretching $\Delta tU_w/h = 235$) respectively. The trough and peak instants are noted by dots in (a) at the top of this figure. The contours in (d) and (e) are both $x$-dependent with bubbles and inertial particles ($\rho_p/\rho_f = 5$), respectively.

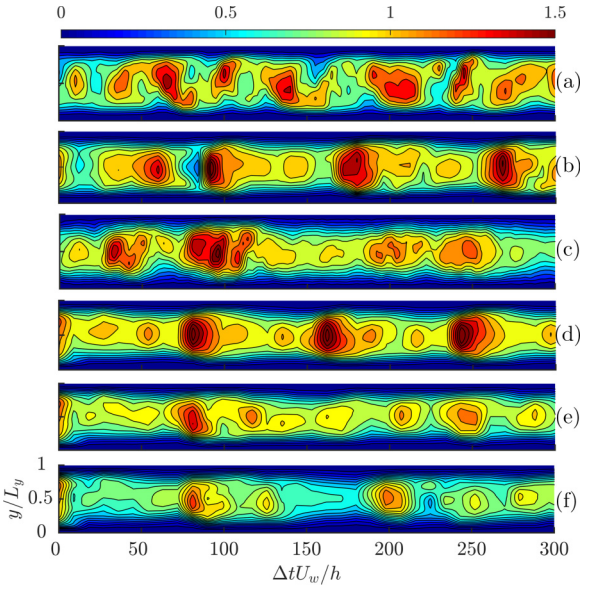


FIG. 25. Evolution in time of shear Reynolds stress $\overline{u'^+v'^+}(y,t)$ averaged over the homogeneous directions. (a), (b) For single-phase flow at $\mathrm{Re}_b = 500$ and 380, respectively. (c)–(f) Corresponding to two-phase flow simulations at $\mathrm{Re}_b = 500$, $\Phi = 10\%$, and different particle size and inertia. (c) $L_y/d = 10$ and $\rho_p/\rho_f = 1$. (d) $L_y/d = 20$ and bubbles are used. (e) $L_y/d = 20$ and $\rho_p/\rho_f = 2$. (f) $L_y/d = 20$ and $\rho_p/\rho_f = 5$.

velocity-defect law. In pCf, the existence of the LSVs leads to a strong coupling between the two low-speed streaks generated by the two walls with opposite velocities. The low-speed streak will extend to the other wall acting as the high-speed streak on this wall. These two low-speed streaks promote each other while LSVs are located in the core of pCf. These different coherent structures also determine the different locations and periodicity of ejection events for these two configurations. Comparing Fig. 1 in Ref. [26] to Fig. 25, in channel flow, the intervals between ejection events are distributed intermittently and close to the boundary, whereas they are quasiperiodic and located in the core region for pCf.

## VII. CONCLUSION

In this study we addressed the effect of finite-size particles on turbulent plane Couette flow, at moderate concentration. The Reynolds numbers considered were close to the laminar-turbulent transition, such that large-scale rotational structures were well developed and self-sustained. Thereby, interaction of particles with coherent structures could be evidenced using particle-resolved numerical simulations with two Couette gap-to-particle size ratios (10 and 20), and with particle-to-fluid density ratio ranging from 0 to 5. The average settling induced by gravity forces was neglected to focus on the interactions induced by the sheared or strained flow. Careful tests were carried out to verify the numerical method accuracy in the range of particle Reynolds and Stokes numbers up to 10, which corresponds to turbulent suspension flow configuration.

Regarding the distribution of particles, the volumetric concentration profiles (averaged in the homogeneous streamwise and spanwise directions) have shown a homogeneous distribution of particles across the Couette gap, resulting from the balance between hydrodynamic repulsive force from the walls, turbulent mixing, and shear-induced diffusion. In the case of neutrally buoyant particles, 2D snapshots of particle positions revealed higher (resp. lower) presence of particles in the sweep (resp. ejection) regions where they are periodically trapped (resp. expelled). Light particles ($\rho_p/\rho_f < 1$) were experiencing, in addition to the above-mentioned flow interactions, an inertia-induced lift force towards the center of large-scale vortices. This led to an increase of the concentration in the Couette center. On the contrary, inertial particles ($\rho_p/\rho_f > 1$), were rather moving towards the walls, leading to small localized peaks in the concentration profile in that region.

Time-averaged profiles, in the wall-normal direction, of the mean flow and Reynolds stress components did not reveal significant difference between single-phase and two-phase flows at equivalent effective Reynolds number, except that the wall shear stress is higher for the two-phase flow. However temporal and modal analysis of flow fluctuations, suggested that particles had an effect on the regeneration cycle of turbulence. While the energy of large-scale vortices (LSVs) was unchanged by particles (only the rotation rate inside the vortex core was slightly reduced), the level of kinetic energy was increased over the range of intermediate wave numbers for all considered particle sizes and densities. This is mainly due to flow perturbations induced by the nondeformability of the dispersed phase (finite-size effect). The shape of the streaks was altered by particles, with an increased probability of strong streamwise fluctuations with the largest particles and reduction of the range of streamwise fluctuations by the heaviest ones. The modal analysis of velocity fluctuations revealed that particles had also an effect on the streak dynamics. The intermittent character of the flow was modified by the particle presence: the amplitude of fluctuations was reduced and the period was modified especially by the largest particles. Similarly to the modal energy, the average value of the circulation was kept unchanged, whereas its standard deviation was reduced when particle inertia was increased.

## ACKNOWLEDGMENTS

This work was granted access to the HPC resources of CALMIP under the allocation 2015 and 2016-P1002 and of GENCI under the allocation x20162b6942. We are grateful to COST Action MP1305 on Flowing Matter. G.W. would like to thank J. Feng, L. Brandt, and O. Masbernat for

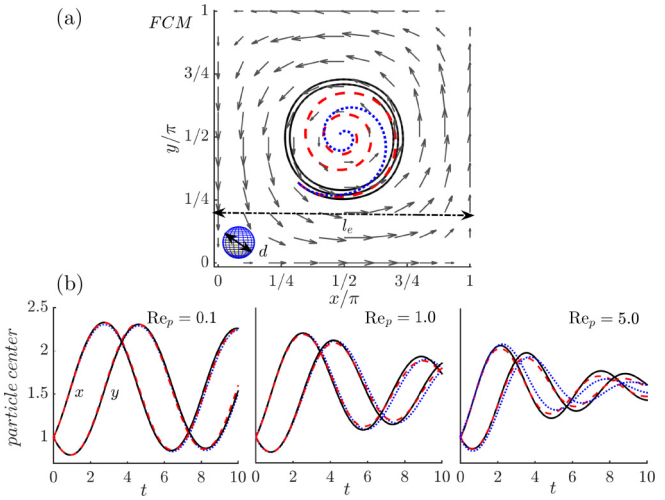


FIG. 26. Trajectory of a bubble ($\rho_p/\rho_f = 1.257 \times 10^{-3}$) in a Taylor-Green vortex at different $\mathrm{Re}_p$. (a) Trajectory in $x$-$y$ plane. ——— $\mathrm{Re}_p = 0.1$; – – – $\mathrm{Re}_p = 1.0$; ..... $\mathrm{Re}_p = 5.0$. (b) Comparison of the FCM results with the numerical solution of Eq. (A1): ——— Eq. (A1); – – – Eq. (A1) with adding the lift force from Eq. (A3) and Eq. (A2); ..... present simulation.

helpful discussions on the particle migration, regeneration cycle laden with finite-size particles, and particle suspension dynamics, respectively. Great help from A. Pedrono for technical support on JADIM is also acknowledged.

## APPENDIX A: EFFECT OF INERTIA ON PARTICLE DYNAMICS IN TAYLOR-GREEN VORTEX

In rotational flows, particles are known to exhibit preferential concentration in vortices that depends on their inertia: bubbles accumulate in low-pressure regions (center of a vortex), whereas heavy particles are expelled towards high-strain regions. To test the ability of FCM to predict the correct particle motion across flow streamlines for different particle inertia, we performed numerical simulations using a single finite-size particles in a periodic Taylor-Green vortex array. Figure 26 shows the particle trajectory in a Taylor-Green vortex for different particle-to-fluid density ratios and different particle $\mathrm{Re}_p$, with a particle-to-vortex size ratio $d/l_e = 0.4/\pi$. The behavior of light and heavy particles is correctly captured by FCM: bubbles move towards the vortex center and inertial particles are pushed towards the high-strain rate regions (not shown here). Only the motion of bubbles is illustrated in Fig. 26 for different Reynolds numbers. The higher the Reynolds number, the faster is the inward spiraling motion.

Numerical results were compared to the trajectory of a single particle predicted by the Maxey-Riley equation [44] written for point particles (of radius $a$ and mass $m_p$) at low Reynolds number:

$$m_p \frac{d\boldsymbol{u}_p}{dt} = m_f \frac{D\boldsymbol{u}_f}{Dt} - \frac{m_f}{2}\left(\frac{d\boldsymbol{u}_p}{dt} - \frac{D\boldsymbol{u}_f}{Dt}\right) - 6\pi a_p \rho_f \nu(\boldsymbol{u}_p - \boldsymbol{u}_f) - 6a_p^2 \rho_f \sqrt{\pi \nu} \int_{t_0}^{t} \frac{1}{\sqrt{t-\tau}}\left(\frac{d\boldsymbol{u}_p}{d\tau} - \frac{d\boldsymbol{u}_f}{d\tau}\right). \tag{A1}$$

In Eq. (A1) the Faxén terms due to velocity curvature in the added mass, drag, and Basset contributions are neglected. Equation (A1) was solved using the Adams-Bashforth multistep integral method with an explicit scheme for the Basset history force (following Daitche [13]), the accuracy of this scheme being second order in time. The numerical integration of Eq. (A1) was tested against the

analytical solution of Ref. [10] to calculate particle trajectory in a rigid-body vortex. The agreement was very good.

The single particle trajectory in a Taylor-Green vortex from FCM simulations is very well predicted by Maxey-Riley equation of motion at $\mathrm{Re}_p = 0.1$. At higher $\mathrm{Re}_p$, the agreement is good during the first period of rotation. Then discrepancy builds in following periods. Adding Faxen terms (except for the history contribution) did not have any significant impact on particle trajectory.

The Maxey-Riley equation of motion does not contain the lift force due to shear of the undisturbed flow. This force perpendicular to the particle slip velocity is negligible at low Reynolds numbers and becomes significant when $\mathrm{Re}_p$ increases. Its analytical expression is somehow complicated to derive in a general flow configuration, because the contribution of convective and unsteady terms to this force are not additive due to nonlinearity [9]. However we can use the model proposed in Saffman's work [58] in the limit of low but finite Reynolds number based on the particle slip velocity $(\boldsymbol{u}_f - \boldsymbol{u}_p)$ with respect to the unperturbed fluid flow velocity $u_f$:

$$\boldsymbol{F}_{L(Sa)} = -6.45\rho_f \nu a^2 \left(\frac{\nu}{|\boldsymbol{\Omega}|}\right)^{\frac{1}{2}} \boldsymbol{\Omega} \times (\boldsymbol{u}_f - \boldsymbol{u}_p). \tag{A2}$$

$\boldsymbol{\Omega} = \boldsymbol{\nabla} \times \boldsymbol{u}_f$ is the flow vorticity. An extension of this lift force can be found in Mei [45] at finite particle Reynolds number ($\mathrm{Re}_s \leqslant 40$) fitting the numerical results reported in Dandy and Dwyer [14]:

$$\frac{F_L}{F_{L(Sa)}} = (1 - 0.3314\alpha^{0.5}) \exp\left(-\frac{\mathrm{Re}_s}{10}\right) + 0.3314\alpha^{0.5}, \tag{A3}$$

where $\mathrm{Re}_s$ is a Reynolds number based on the slip velocity $\mathrm{Re}_S = \frac{|u_f - u_p|2a}{\nu}$ and $\alpha$ is a dimensionless shear rate $\alpha = \frac{|\partial u_f/\partial y|a}{|u_f - u_p|}$.

Adding the lift force to the Maxey-Riley equation reduces the overestimate of the theoretical prediction, but it did not match exactly the numerical evolution obtained with FCM.

## APPENDIX B: SHEAR STRESS BUDGET

The stress of a suspension flow has been derived by Batchelor [4] assuming homogeneous conditions. Batchelor introduced a decomposition of the stress into fluid and particulate phase contributions $\Sigma_{ij} = \Sigma_{ij}^{(f)} + \Sigma_{ij}^{(p)}$ where both terms are explicitly written as (the dispersed phase has total surface $\Sigma A_0$ and volume $\Sigma V_0$)

$$\Sigma_{ij}^{(f)} = \underbrace{\frac{1}{V}\int_{V-\sum V_0} \left[\mu\left(\frac{\partial u_i}{\partial x_j} + \frac{\partial u_j}{\partial x_i}\right)\right] dV}_{\tau_v, \text{viscous stress}} - \underbrace{\frac{1}{V}\int_{V-\sum V_0} \rho u_i' u_j' \, dV}_{\tau_{T_f}, \text{ fluid Reynolds stress}}, \tag{B1}$$

$$\Sigma_{ij}^{(p)} = \underbrace{\frac{1}{V}\sum \frac{1}{2}\int_{A_0} \left[\sigma_{ik}x_j + \sigma_{jk}x_i\right] n_k \, dA}_{\tau_s, \text{ particle stresslet}} + \underbrace{\frac{1}{V}\sum \frac{1}{2}\int_{A_0} \left[\sigma_{ik}x_j - \sigma_{jk}x_i\right] n_k \, dA}_{\text{particle rotlet}}$$
$$- \underbrace{\frac{1}{V}\int_{\sum V_0} \rho f_i' x_j \, dV}_{\text{stress due to particle acceleration}} - \underbrace{\frac{1}{V}\int_{\sum V_0} \rho u_i' u_j' \, dV}_{\tau_{T_p}, \text{ particle Reynolds stress}}. \tag{B2}$$

In the absence of external torques and forces applied on particles, the first and last terms of Eq. (B2) account for the contribution of particles to the total stress. Note that the Reynolds stress components in the work of Batchelor appear only inside the particle contribution because the flow is laminar. Here the Reynolds stress appears also in the stress of the fluid phase due to the flow

TABLE III. Contributions to the Reynolds-stress transport Eq. (C2) and Eq. (C3)

| | $\overline{u}^2$ | $\overline{u'u'}$ | $\overline{v'v'}$ | $\overline{w'w'}$ | $\overline{u'v'}$ |
|---|---|---|---|---|---|
| $P_{ij}$ | $\rho\overline{u'v'}\frac{d\overline{u}}{dy}$ | $-\rho\overline{u'v'}\frac{d\overline{u}}{dy}$ | – | – | $-\rho\overline{v'v'}\frac{d\overline{u}}{dy}$ |
| $\varepsilon_{ij}$ | $-\mu(\frac{d\overline{u}}{dy})^2$ | $-\mu\overline{\frac{\partial u'}{\partial x_j}\frac{\partial u'}{\partial x_j}}$ | $-\mu\overline{\frac{\partial v'}{\partial x_j}\frac{\partial v'}{\partial x_j}}$ | $-\mu\overline{\frac{\partial w'}{\partial x_j}\frac{\partial w'}{\partial x_j}}$ | $-2\mu\overline{\frac{\partial u'}{\partial x_j}\frac{\partial v'}{\partial x_j}}$ |
| $T_{ij}$ | $-\rho\frac{d}{dy}(\overline{u'v'u})$ | $-\rho\frac{\partial}{\partial y}(\frac{1}{2}\overline{u'^2v'})$ | $\rho\frac{\partial}{\partial y}(\frac{1}{2}\overline{v'^3})$ | $\rho\frac{\partial}{\partial y}(\frac{1}{2}\overline{w'^2v'})$ | $-\rho\frac{\partial}{\partial x_j}(\overline{u'v'u'_j})$ |
| $\Pi^s_{ij}$ | $\overline{p}\frac{d\overline{u}}{dx}$ | $\overline{p'\frac{\partial u'}{\partial x}}$ | $\overline{p'\frac{\partial v'}{\partial y}}$ | $\overline{p'\frac{\partial w'}{\partial z}}$ | $\overline{p'(\frac{\partial v'}{\partial x}+\frac{\partial u'}{\partial y})}$ |
| $\Pi^d_{ij}$ | $-\frac{d\overline{pu}}{dx}$ | $-\overline{\frac{\partial p'u'}{\partial x}}$ | $-\overline{\frac{\partial p'v'}{\partial y}}$ | $-\overline{\frac{\partial p'w'}{\partial z}}$ | $-\overline{(\frac{\partial p'v'}{\partial x}+\frac{\partial p'u'}{\partial y})}$ |
| $D_{ij}$ | $\mu\frac{d^2}{dy^2}(\frac{1}{2}\overline{u}^2)$ | $\mu\frac{\partial^2}{\partial y^2}(\frac{1}{2}\overline{u'^2})$ | $\mu\frac{\partial^2}{\partial y^2}(\frac{1}{2}\overline{v'^2})$ | $\mu\frac{\partial^2}{\partial y^2}(\frac{1}{2}\overline{w'^2})$ | $\mu\frac{\partial^2}{\partial x_j^2}(\overline{u'v'})$ |
| $FB^m_{ij}$ | $\overline{u}\,\overline{f_m(x)}$ | $\overline{u'f'_m(x)}$ | $\overline{v'f'_m(y)}$ | $\overline{w'f'_m(z)}$ | $\overline{u'f'_m(y)}+\overline{v'f'_m(x)}$ |
| $FB^d_{ij}$ | $\overline{u}\,\overline{f_d(x)}$ | $\overline{u'f'_d(x)}$ | $\overline{v'f'_d(y)}$ | $\overline{w'f'_d(z)}$ | $\overline{u'f'_d(y)}+\overline{v'f'_d(x)}$ |

turbulence. To summarize,the stress budget is

$$\tau_{\text{total}} = \tau_v + \tau_{T_f} + \tau_s + \tau_{T_p} \tag{B3}$$

similarly to what has been written in Ref. [49] following Ref, [72]. When scaled by the wall shear stress $\tau_w$, this budget writes

$$\tau^+_{\text{total}} = 1 = \tau^+_v + \tau^+_{T_f} + \tau^+_s + \tau^+_{T_p} \tag{B4}$$

## APPENDIX C: REYNOLDS STRESS BUDGET

The Reynolds stress budget was obtained starting from the Navier-Stokes equations coupled to particle volume forcing terms derived from the FCM:

$$\rho\left(\frac{\partial u_i}{\partial t} + u_j\frac{\partial u_i}{\partial x_j}\right) = -\frac{\partial p}{\partial x_j} + \mu\frac{\partial^2 u_i}{\partial x_i\partial x_j} + f_m(x_i,t) + f_d(x_i,t). \tag{C1}$$

Here $f_m$ and $f_d$ correspond to monopole and dipole forces, respectively. Multiplying Eq. (C1) by the fluid velocity and subtracting the mean energy balance equation, one can obtain the balance for the flow velocity fluctuations or Reynolds stress. The Reynolds stress and mean energy balances are written as

$$\rho\left(\frac{\partial}{\partial t}\overline{u'_iu'_j} + \overline{u_k}\frac{\partial}{\partial x_k}\overline{u'_iu'_j}\right) = \overline{P'}_{ij} - \overline{\varepsilon'_{ij}} + \overline{T'_{ij}} + \overline{\Pi'_{ij}} + \overline{D'_{ij}} + \overline{FB'_{ij}}, \tag{C2}$$

$$\rho\left[\frac{\partial}{\partial t}\left(\frac{1}{2}\overline{u_i}\,\overline{u_i}\right) + \overline{u_j}\frac{\partial}{\partial x_j}\left(\frac{1}{2}\overline{u_i}\,\overline{u_i}\right)\right] = \overline{P_{ij}} - \overline{\varepsilon_{ij}} + \overline{T_{ij}} + \overline{\Pi_{ij}} + \overline{D_{ij}} + \overline{FB_{ij}}. \tag{C3}$$

A prime symbol is added to all fluctuating components. The expressions of the contributions on the right-hand side of Eq. (C2) and Eq. (C3) are written in Table III.

The Reynolds stress budgets allow to obtain the rate of change of both normal and off-diagonal Reynolds stress terms. As stated by Jeong *et al.* [27], energy is extracted from the mean flow large-scale vortices to $u'u'$ due to advection. Intercomponent energy transfer (from $u'u'$ to $v'v'$ and $w'w'$) occurs by vortex stretching and reorientation of vorticity from the mean flow.

In the feedback term $FB_{ij}$ derived from the source term in Navier-Stokes equations, the main contribution comes from the dipole forcing (stresslets) due to particle rigidity. The monopole term is different from zero only when two particles are close to contact, and its contribution to the balances [Eq. (C2) and Eq. (C3)] is negligible in the range of concentrations considered in this work.

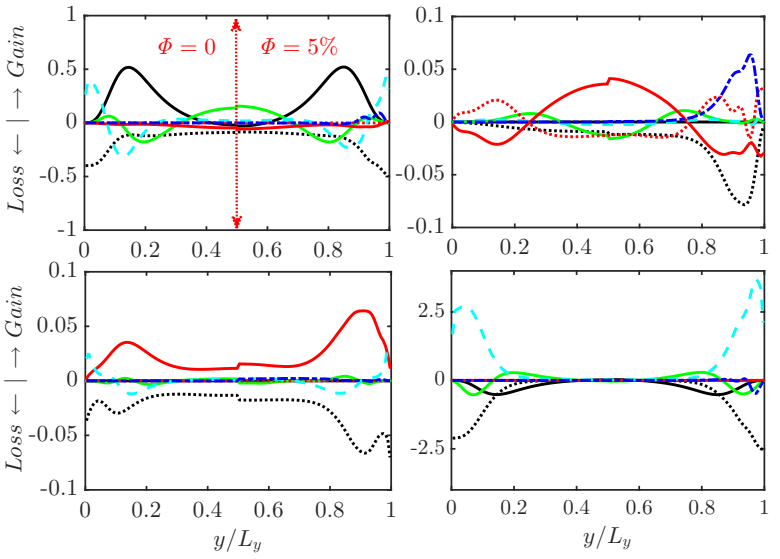


FIG. 27. Contributions to the budget of (a) $\overline{u'u'}$, (b) $\overline{v'v'}$, (c) $\overline{w'w'}$, and (d) $\overline{u}\,\overline{u}$ in the case of $\mathrm{Re}_b = 500$ and $L_y/d = 20$. Comparison between single-phase and $\phi = 5\%$ suspension flow. Because of symmetry of profiles, in each figure the left part correspond to single-phase flow and the right part stands for two-phase flows. —— production; ..... dissipation; —— turbulent transport; —— pressure strain; ..... pressure diffusion; – – – viscous diffusion; – – – dipole feedback.

Different contributions to Reynolds stress and mean flow budgets are plotted in Fig. 27. In two-phase flow, the sign of all contributions is not changed with respect to the reference single-phase flow case. It is observed that particles mainly increase the rate of energy dissipation in all directions. Other observations can be summarized as follows:

(1) $\overline{P'_{11}}$ is the only term that extracts energy from the mean flow to produce $\overline{u'u'}$. This production term is almost unchanged by particles.

(2) $\overline{FB'_{22}}$ injects energy in $\overline{v'v'}$. The feedback term is maximum near the wall where the shear rate is the strongest. It generates the major evident signature of the turbulence modulation by particles.

(3) $\overline{\Pi'^{s}_{33}}$, the source term in the budget of $\overline{w'w'}$, is slightly stronger in two-phase flow.

(4) $\overline{P'_{12}}$ is the main production term of $\overline{u'v'}$ and $\Pi'^{s}_{12}$ is the main sink term. Their respective rates are both increased when particles are added to the flow (see Fig. 27).

[1] M. Abbas, E. Climent, O. Simonin, and M. R. Maxey, Dynamics of bidisperse suspensions under Stokes flows: Linear shear flow and sedimentation, Phys. Fluids **18**, 121504 (2006).

[2] V. Avsarkisov, S. Hoyas, M. Oberlack, and J. García-Galache, Turbulent plane Couette flow at moderately high Reynolds number, J. Fluid Mech. **751**, R1 (2014).

[3] S. Balachandar and J. K. Eaton, Turbulent dispersed multiphase flow, Annu. Rev. Fluid. Mech. **42**, 111 (2010).

[4] G. Batchelor, The stress system in a suspension of force-free particles, J. Fluid Mech. **41**, 545 (1970).

[5] G. K. Batchelor, *An Introduction to Fluid Dynamics* (Cambridge University Press, Cambridge, 2000).

[6] K. H. Bech, N. Tillmark, P. H. Alfredsson, and H. I. Andersson, An investigation of turbulent plane Couette flow at low Reynolds numbers, J. Fluid Mech. **286**, 291 (1995).

[7] T. M. Burton and J. K. Eaton, Fully resolved simulations of particle-turbulence interaction, J. Fluid Mech. **545**, 67 (2005).
[8] I. Calmet and J. Magnaudet, Large-eddy simulation of high-Schmidt number mass transfer in a turbulent channel flow, Phys. Fluids **9**, 438 (1997).
[9] F. Candelier and J. Angilella, Analytical investigation of the combined effect of fluid inertia and unsteadiness on low-Re particle centrifugation, Phys. Rev. E **73**, 047301 (2006).
[10] F. Candelier, J. Angilella, and M. Souhar, On the effect of the Boussinesq-Basset force on the radial migration of a Stokes particle in a vortex, Phys. Fluids **16**, 1765 (2004).
[11] E. Climent and M. Maxey, Numerical simulations of random suspensions at finite Reynolds numbers, Int. J. Multiphase Flow **29**, 579 (2003).
[12] E. Climent and M. R. Maxey, The force coupling method: A flexible approach for the simulation of particulate flows, in *Theoretical Methods for Micro Scale Viscous Flows*, edited by F. Feuillebois and A. Sellier (Transworld Research World, 2009).
[13] A. Daitche, Advection of inertial particles in the presence of the history force: Higher order numerical schemes, J. Comput. Phys. **254**, 93 (2013).
[14] D. S. Dandy and H. A. Dwyer, A sphere in shear flow at finite Reynolds number: Effect of shear on particle lift, drag, and heat transfer, J. Fluid Mech. **216**, 381 (1990).
[15] J. B. de Motta, W.-P. Breugem, B. Gazanion, J.-L. Estivalezes, S. Vincent, and E. Climent, Numerical modeling of finite-size particle collisions in a viscous fluid, Phys. Fluids **25**, 083302 (2013).
[16] C. D. Dritselis and N. S. Vlachos, Numerical study of educed coherent structures in the near-wall region of a particle-laden channel flow, Phys. Fluids **20**, 055103 (2008).
[17] Y. Duguet, P. Schlatter, and D. S. Henningson, Formation of turbulent patterns near the onset of transition in plane Couette flow, J. Fluid Mech. **650**, 119 (2010).
[18] S. Elghobashi and G. Truesdell, On the two-way interaction between homogeneous turbulence and dispersed solid particles. I: Turbulence modification, Phys. Fluids A **5**, 1790 (1993).
[19] J. Feng, H. Hu, and D. Joseph, Direct simulation of initial value problems for the motion of solid bodies in a Newtonian fluid. Part 2. Couette and Poiseuille flows, J. Fluid Mech. **277**, 271 (1994).
[20] R. Gore and C. T. Crowe, Effect of particle size on modulating turbulent intensity, Int. J. Multiphase Flow **15**, 279 (1989).
[21] H. Haddadi and J. F. Morris, Microstructure and rheology of finite inertia neutrally buoyant suspensions, J. Fluid Mech. **749**, 431 (2014).
[22] J. Halow and G. Wills, Radial migration of spherical particles in Couette systems, AIChE J. **16**, 281 (1970).
[23] J. M. Hamilton and F. H. Abernathy, Streamwise vortices and transition to turbulence, J. Fluid Mech. **264**, 185 (1994).
[24] J. M. Hamilton, J. Kim, and F. Waleffe, Regeneration mechanisms of near-wall turbulence structures, J. Fluid Mech. **287**, 317 (1995).
[25] B. Ho and L. Leal, Inertial migration of rigid spheres in two-dimensional unidirectional flows, J. Fluid Mech. **65**, 365 (1974).
[26] T. Itano and S. Toh, The dynamics of bursting process in wall turbulence, J. Phys. Soc. Jpn. **70**, 703 (2001).
[27] J. Jeong, F. Hussain, W. Schoppa, and J. Kim, Coherent structures near the wall in a turbulent channel flow, J. Fluid Mech. **332**, 185 (1997).
[28] J. Jiménez and P. Moin, The minimal flow unit in near-wall turbulence, J. Fluid Mech. **225**, 213 (1991).
[29] G. Kawahara and S. Kida, Periodic motion embedded in plane Couette turbulence: Regeneration cycle and burst, J. Fluid Mech. **449**, 291 (2001).
[30] J. Klinkenberg, G. Sardina, H. De Lange, and L. Brandt, Numerical study of laminar-turbulent transition in particle-laden channel flow, Phys. Rev. E **87**, 043011 (2013).
[31] J. Komminaho, A. Lundbladh, and A. V. Johansson, Very large structures in plane turbulent Couette flow, J. Fluid Mech. **320**, 259 (1996).
[32] J. D. Kulick, J. R. Fessler, and J. K. Eaton, Particle response and turbulence modification in fully developed channel flow, J. Fluid Mech. **277**, 109 (1994).

[33] P. M. Kulkarni and J. F. Morris, Suspension properties at finite Reynolds number from simulated shear flow, Phys. Fluids **20**, 040602 (2008).
[34] I. Lashgari, F. Picano, W.-P. Breugem, and L. Brandt, Laminar, Turbulent, and Inertial Shear-Thickening Regimes in Channel Flow of Neutrally Buoyant Particle Suspensions, Phys. Rev. Lett. **113**, 254502 (2014).
[35] M. J. Lee and J. Kim, The structure of turbulence in a simulated plane Couette flow, in *Proceedings of the 8th Symposium on Turbulent Shear Flows* (1991), http://turb.seas.ucla.edu/∼jkim/papers/couette.pdf.
[36] Y. Li, J. B. McLaughlin, K. Kontomaris, and L. Portela, Numerical simulation of particle-laden turbulent channel flow, Phys. Fluids **13**, 2957 (2001).
[37] V. Loisel, M. Abbas, O. Masbernat, and E. Climent, The effect of neutrally buoyant finite-size particles on channel flows in the laminar-turbulent transition regime, Phys. Fluids **25**, 123304 (2013).
[38] V. Loisel, M. Abbas, O. Masbernat, and E. Climent, Inertia-driven particle migration and mixing in a wall-bounded laminar suspension flow, Phys. Fluids **27**, 123304 (2015).
[39] S. Lomholt and M. R. Maxey, Force-coupling method for particulate two-phase flow: Stokes flow, J. Comput. Phys. **184**, 381 (2003).
[40] J.-P. Matas, J. F. Morris, and E. Guazzelli, Transition to Turbulence in Particulate Pipe Flow, Phys. Rev. Lett. **90**, 014501 (2003).
[41] M. Maxey, Examples of fluid-particle interactions in dispersed two-phase flow, in *Proceedings of the 30th AIAA Fluid Dynamics Conference, Norfolk, VA* (AIAA, 1999), pp. 1–5.
[42] M. Maxey, Simulation methods for particulate flows and concentrated suspensions, Annu. Rev. Fluid. Mech. **49**, 171 (2017).
[43] M. Maxey and B. Patel, Localized force representations for particles sedimenting in Stokes flow, Int. J. Multiphase Flow **27**, 1603 (2001).
[44] M. R. Maxey and J. J. Riley, Equation of motion for a small rigid sphere in a nonuniform flow, Phys. Fluids **26**, 883 (1983).
[45] R. Mei, An approximate expression for the shear lift force on a spherical particle at finite Reynolds number, Int. J. Multiphase Flow **18**, 145 (1992).
[46] D. R. Mikulencak and J. F. Morris, Stationary shear flow around fixed and free bodies at finite Reynolds number, J. Fluid Mech. **520**, 215 (2004).
[47] S. S. Ozarkar and A. S. Sangani, A method for determining Stokes flow around particles near a wall or in a thin film bounded by a wall and a gas-liquid interface, Phys. Fluids **20**, 063301 (2008).
[48] Y. Pan and S. Banerjee, Numerical simulation of particle interactions with wall turbulence, Phys. Fluids **8**, 2733 (1996).
[49] F. Picano, W.-P. Breugem, and L. Brandt, Turbulent channel flow of dense suspensions of neutrally buoyant spheres, J. Fluid Mech. **764**, 463 (2015).
[50] S. Pirozzoli, M. Bernardini, and P. Orlandi, Turbulence statistics in Couette flow at high Reynolds number, J. Fluid Mech. **758**, 327 (2014).
[51] M. Rashidi, G. Hetsroni, and S. Banerjee, Particle-turbulence interaction in a boundary layer, Int. J. Multiphase Flow **16**, 935 (1990).
[52] H. Reichardt, Über die Geschwindigkeitsverteilung in einer geradlinigen turbulenten Couetteströmung, J. Appl. Math. Mech./Z. Angew. Math. Mech. **36**, S26 (1956).
[53] D. H. Richter, Turbulence modification by inertial particles and its influence on the spectral energy budget in planar Couette flow, Phys. Fluids **27**, 063304 (2015).
[54] D. H. Richter and P. P. Sullivan, Momentum transfer in a turbulent, particle-laden Couette flow, Phys. Fluids **25**, 053304 (2013).
[55] D. H. Richter and P. P. Sullivan, Modification of near-wall coherent structures by inertial particles, Phys. Fluids **26**, 103304 (2014).
[56] S. K. Robinson, A review of vortex structures and associated coherent motions in turbulent boundary layers, in *Structure of Turbulence and Drag Reduction* (Springer, New York, 1990), pp. 23–50.
[57] C. Rogers and J. Eaton, The effect of small particles on fluid turbulence in a flat-plate, turbulent boundary layer in air, Phys. Fluids A **3**, 928 (1991).
[58] P. Saffman, The lift on a small sphere in a slow shear flow, J. Fluid Mech. **22**, 385 (1965).

[59] A. S. Sangani, A. Acrivos, and P. Peyla, Roles of particle-wall and particle-particle interactions in highly confined suspensions of spherical particles being sheared at low Reynolds numbers, Phys. Fluids **23**, 083302 (2011).
[60] W. Schoppa and F. Hussain, Coherent structure generation in near-wall turbulence, J. Fluid Mech. **453**, 57 (2002).
[61] X. Shao, T. Wu, and Z. Yu, Fully resolved numerical simulation of particle-laden turbulent flow in a horizontal channel at a low Reynolds number, J. Fluid Mech. **693**, 319 (2012).
[62] G. Subramanian, D. L. Koch, J. Zhang, and C. Yang, The influence of the inertially dominated outer region on the rheology of a dilute dispersion of low-Reynolds-number drops or rigid particles, J. Fluid Mech. **674**, 307 (2011).
[63] T. Tanaka and J. K. Eaton, Sub-Kolmogorov resolution partical image velocimetry measurements of particle-laden forced turbulence, J. Fluid Mech. **643**, 177 (2010).
[64] N. Tillmark and P. H. Alfredsson, Experiments on transition in plane Couette flow, J. Fluid Mech. **235**, 89 (1992).
[65] T. Tsukahara, H. Kawamura, and K. Shingai, DNS of turbulent Couette flow with emphasis on the large-scale structure in the core region, J. Turbul **7**, N19 (2006).
[66] P. Vasseur and R. Cox, The lateral migration of a spherical particle in two-dimensional shear flows, J. Fluid Mech. **78**, 385 (1976).
[67] F. Waleffe, On a self-sustaining process in shear flows, Phys. Fluids **9**, 883 (1997).
[68] F. Waleffe, J. Kim, and J. M. Hamilton, On the origin of streaks in turbulent shear flows, in *Turbulent Shear Flows 8* (Springer, New York, 1993), pp. 37–49.
[69] K. Yeo and M. R. Maxey, Dynamics and rheology of concentrated, finite-Reynolds-number suspensions in a homogeneous shear flow, Phys. Fluids **25**, 053303 (2013).
[70] Z. Yu, T. Wu, X. Shao, and J. Lin, Numerical studies of the effects of large neutrally buoyant particles on the flow instability and transition to turbulence in pipe flow, Phys. Fluids **25**, 043305 (2013).
[71] B. Yung, H. Merry, and T. Bott, The role of turbulent bursts in particle re-entrainment in aqueous systems, Chem. Eng. Sci. **44**, 873 (1989).
[72] Q. Zhang and A. Prosperetti, Physics-based analysis of the hydrodynamic stress in a fluid-particle system, Phys. Fluids **22**, 033306 (2010).
[73] L. Zhao, H. I. Andersson, and J. J. Gillissen, Interphasial energy transfer and particle dissipation in particle-laden wall turbulence, J. Fluid Mech. **715**, 32 (2013).